

Direct numerical simulations of two- and three-dimensional turbulent natural convection flows in a differentially heated cavity of aspect ratio 4

F. X. TRIAS, M. SORIA, A. OLIVA
AND C. D. PÉREZ-SEGARRA

Centre Tecnològic de Transferència de Calor (CTTC) Universitat Politècnica de Catalunya (UPC),
c/ Colom 11, 08222 Terrassa, Spain

(Received 15 February 2006 and in revised form 18 April 2007)

A set of complete two- and three-dimensional direct numerical simulations (DNS) in a differentially heated air-filled cavity of aspect ratio 4 with adiabatic horizontal walls is presented in this paper. Although the physical phenomenon is three-dimensional, owing to its prohibitive computational costs the majority of the previous DNS of turbulent and transition natural convection flows in enclosed cavities assumed a two-dimensional behaviour. The configurations selected here (Rayleigh number based on the cavity height 6.4×10^8 , 2×10^9 and 10^{10} , $Pr = 0.71$) are an extension to three dimensions of previous two-dimensional problems.

An overview of the numerical algorithm and the methodology used to verify the code and the simulations is presented. The main features of the flow, including the time-averaged flow structure, the power spectra and probability density distributions of a set of selected monitoring points, the turbulent statistics, the global kinetic energy balances and the internal waves motion phenomenon are described and discussed.

As expected, significant differences are observed between two- and three-dimensional results. For two-dimensional simulations the oscillations at the downstream part of the vertical boundary layer are clearly stronger, ejecting large eddies to the cavity core. In the three-dimensional simulations these large eddies do not persist and their energy is rapidly passed down to smaller scales of motion. It yields on a reduction of the large-scale mixing effect at the hot upper and cold lower regions and consequently the cavity core still remains almost motionless even for the highest Rayleigh number. The boundary layers remain laminar in their upstream parts up to the point where these eddies are ejected. The point where this phenomenon occurs clearly moves upstream for the three-dimensional simulations. It is also shown that, even for the three-dimensional simulations, these eddies are large enough to permanently excite an internal wave motion in the stratified core region. All these differences become more marked for the highest Rayleigh number.

1. Introduction

Natural convection in parallelepipedic enclosures has been the subject of numerous studies. Most of them can be classified in three main groups: cavities where the flow is due to internal heat generation, cavities heated from below (Rayleigh–Bénard configuration), and those heated from the sides. The configuration of the latter class

is the differentially heated cavity, the situation that here is under consideration. This models many engineering applications such as ventilation of rooms, cooling of electronic devices or air flow in buildings. A summary of previous direct numerical simulations of air-filled ($Pr = 0.71$) differentially heated cavities relevant in our context is presented in the following. The coordinate system used is: x_1 for the periodic direction and x_2 (horizontal) and x_3 (vertical) for the two wall-normal directions. Ra_2 and Ra_3 are the Rayleigh numbers based on the cavity width and height, respectively. $A_3 = L_3/L_2$ and $A_1 = L_1/L_2$ are the height and depth aspect ratios. Unless otherwise mentioned, all cases use Boussinesq approximation.

The early numerical studies concentrated on configurations characterized by small Rayleigh numbers in the steady laminar regime. After the pioneering work of de Vahl Davis & Jones (1983), where the original benchmark formulation was established for a set of square two-dimensional cavities with $10^3 \leq Ra \leq 10^6$, Hortmann, Peric & Scheuerer (1990) used a multigrid method to solve the problem with finer meshes up to 640×640 . Latter, solutions for the full range of two-dimensional steady-state solutions ($Ra_3 \leq 10^8$) were obtained using different methods by Le Quéré (1991), Ravi, Henkes & Hoogendoorn (1994) and Wan, Patnaik & Wei (2001). The three-dimensional cubic cavity ($A_1 = A_3 = 1$), with adiabatic horizontal walls and solid vertical walls in the third direction is also a well-known configuration, but has received comparatively less attention (see Fusegi *et al.* 1991; Tric, Labrosse & Betrouni 2000). For large height aspect ratio cavities, in a certain range of Ra numbers, a steady-state multicellular flow is obtained (see Lartigue, Lorente & Bourret 2000; Le Quéré 1990; Schweiger *et al.* 1995).

Beyond a critical Rayleigh number, the two-dimensional differentially heated cavity flows become time-dependent (periodic, chaotic and eventually fully turbulent). Owing to the presence of high temperature areas at the bottom of the cavity, the configuration with perfectly conducting horizontal walls is more unstable than the configuration with adiabatic ones. Its transition to non-steadiness was studied by Winters (1987), obtaining a critical number of $Ra_3 = 2.109 \times 10^6$, later confirmed by Henkes (1995). For the square cavity with adiabatic horizontal walls, Le Quéré & Behnia (1998) determined the critical number as $Ra = 1.82 \pm 0.01 \times 10^8$ and studied the time-dependent chaotic flows up to $Ra = 10^{10}$. For the case of cavities also with adiabatic horizontal walls and height aspect ratio $A_3 = 4$, Le Quéré (1994) determined that there is a Hopf bifurcation at $Ra_3 = 1.03 \times 10^8$ and that a chaotic behaviour is first observed at $Ra_3 = 2.3 \times 10^8$. Two-dimensional chaotic flows have been studied by Farhangnia, Biringen & Peltiery (1996), who carried out a direct simulation for $Ra_3 = 6.4 \times 10^{10}$ and by Xin & Le Quéré (1995), who studied the situations with $Ra_3 = 6.4 \times 10^8$, 2×10^9 and 10^{10} , recording statistics of the flow for $Ra_3 = 2 \times 10^9$ and 10^{10} . The cavity with $A_3 = 8$, with $Ra_2 = 3.4 \times 10^5$ (unsteady), has been chosen as a test problem (see Christon, Gresho & Sutton 2002, for example). For this configuration, the critical Ra_2 number for the transition to unsteadiness is $Ra_2 = 3.0619 \times 10^5$. Time-dependent two-dimensional flows have also been studied without using the Boussinesq approximation by Paolucci & Chenoweth (1989) and Paolucci (1990), for Rayleigh numbers up to 10^{10} and different aspect ratios.

The transition from a two-dimensional steady laminar to a three-dimensional time-dependent regime was first considered by Jansen, Henkes & Hoogendoorn (1993), for the case of perfectly conducting horizontal walls in a cubic cavity with solid vertical walls and numerically imposing flow symmetries. The critical Ra number was estimated to be between 2.25×10^6 and 2.35×10^6 , larger than the equivalent critical number of a two-dimensional cavity. An oscillatory flow regime was studied by Fusegi,

Hyun & Kuwahara (1992) under the same conditions, without assuming symmetry, for $Ra = 8.5 \times 10^6$. For the case of the adiabatic horizontal walls in a cubic cavity, the transition to unsteadiness was studied by Jansen & Henkes (1996), assuming symmetry. The critical Ra number obtained was between 2.5×10^8 and 3×10^8 . However, Labrosse *et al.* (1997) studied the same configuration without assuming symmetry, obtaining a non-symmetric transition for $Ra = 3.19 \times 10^7$, significantly lower than in the equivalent two-dimensional case. A direct simulation of a turbulent flow with $Ra = 10^{10}$ was carried out by Fusegi *et al.* (1990), using a $62 \times 122 \times 62$ mesh.

In a general differentially heated cavity problem with periodic vertical boundary conditions where the boundary conditions do not force the flow to be three-dimensional, there are three possible flow configurations: two-dimensional steady; two-dimensional unsteady; and three-dimensional unsteady. A question relevant in our context is whether there is a range of Rayleigh numbers where the flow is two-dimensional but unsteady, this is, if the transitions to unsteadiness and three dimensionality are simultaneous. This problem was considered in detail by Henkes & Le Quéré (1996), for square differentially heated cavities ($A_3 = 1$) with adiabatic horizontal walls and perfectly conducting horizontal walls, using periodic vertical boundary conditions in the third direction. In both cases, three-dimensional perturbations were found to be less stable than two-dimensional perturbations, showing that the assumption of bidimensionality is not correct (in time-dependent square differentially heated cavity). A three-dimensional simulation was carried out for $Ra = 10^8$, with perfectly conducting horizontal walls, using $A_1 = 0.1$ with four Fourier modes in the x_1 -direction. Statistics of the flow were recorded and compared with the statistics of the two-dimensional flow. The most significant difference found was an increase of the heat transfer coefficient in the three-dimensional flow. For cavities of height aspect ratio 4, the same question was considered by Penot, N'Dame & Le Quéré (1990). Experimentally, it was found that in a cavity of $A_1 = 1.33$ there is a transition to unsteadiness at $Ra_3 \approx 10^8$ (in good agreement with Xin & Le Quéré 1995). Two-dimensional numerical simulations confirmed this result. However, in a three-dimensional periodic vertical boundary conditions simulation with a slightly lower Rayleigh number, $Ra_3 = 9.6 \times 10^7$, with $A_1 = 1$, the flow was found to be three-dimensional.

In conclusion, these results by Penot *et al.* (1990) and Henkes & Le Quéré (1996) seem to indicate that for $A_3 = 1$ and $A_3 = 4$ (and large enough A_1), the flows would never be unsteady and two-dimensional. However, this conclusion is not valid for other aspect ratios: Xin & Le Quéré (2002) showed that for $A_3 = 8$, the critical number for the transition to unsteadiness is $Ra_2 = 306\,192 \pm 10$, whereas the two-dimensional to three-dimensional transition is observed at a higher Ra_2 number, at least $\approx 3.84 \times 10^5$.

1.1. Motivation and summary of the present work

Concerning the turbulent regime, the state-of-the-art is not yet satisfactory. Although most of the two-dimensional instability mechanics are now well-known (see Le Quéré & Behnia 1998), three-dimensional effects in the turbulent regime are still a challenge. Many experimental studies have been carried out (see Tian & Karayiannis 2000*a, b*; Betts & Bokhtari 2000) providing valuable data for the testing and tuning of turbulence models. However, the three-dimensional structure of the flow is far from being fully characterized and many differences observed between numerical and experimental results remain unexplained. For example, thermal stratification in the cavity core can still not be predicted well and, despite the efforts of Salat *et al.* (2004) to elucidate the origin of the discrepancies between numerical and experimental results,

it is still an open problem. Moreover, for cavities with active lateral walls, most of the three-dimensional direct numerical simulations have been restricted to values of Rayleigh numbers corresponding to the end of the laminar regime or the transitional regime (see Jansen *et al.* 1993; Tric *et al.* 2000). A three-dimensional direct numerical simulation in a differentially heated cavity with adiabatic horizontal walls and periodic vertical boundary conditions with $A_3 = 4$, $Pr = 0.71$ and $Ra_3 = 6.4 \times 10^8$ (Soria *et al.* 2004) has provided valuable data for investigating three-dimensional effects, finding that the general features of the averaged flow do not change significantly if the flow is treated as two-dimensional. The main differences are found near the downstream corners where stronger recirculations occur for the two-dimensional simulation. On the contrary, the second-order statistics are substantially different, specially at the vertical boundary layers where two-dimensional simulation incorrectly predicts very low turbulence values. However, the Rayleigh number studied by Soria *et al.* (2004), which is only approximately 6 times above the critical value, corresponds to a very weak turbulent flow.

The main objective of the present study is to improve our understanding of the dynamics of turbulent convection in a differentially heated cavity for a set of two- and three-dimensional direct numerical simulations with $A_3 = 4$, $Pr = 0.71$, $Ra_3 = 6.4 \times 10^8$, 2×10^9 and 10^{10} (i.e. two orders of magnitude higher than the critical Ra number). These configurations have been selected as a three-dimensional extension of the two-dimensional problems studied in detail by Xin & Le Quéré (1995) and, of course, as the natural next step of the work initiated by Soria *et al.* (2004). Periodic boundary conditions in the x_1 -direction are used because they allow the study of three-dimensional effects due to intrinsic instability of the main flow and not to the boundary conditions. Hence, a uniform mesh in such a direction is suitable. This is an important computational advantage because Fourier-based methods can be used to solve the Poisson equation in one direction. The flow configurations chosen, according to the numerical and experimental results carried out by Penot *et al.* (1990) and Soria *et al.* (2004) (that are confirmed here by the present simulations), are time-dependent and three-dimensional. As expected, all the two-dimensional results are in good agreement with the data provided by Xin & Le Quéré (1995). Moreover, as was pointed out by Salat *et al.* (2004), we also conclude that thermal stratification discrepancies observed between numerical and experimental results cannot be attributed to the two-dimensional assumption.

The present paper is arranged as follows. In the next section, the governing equations and the numerical method are briefly described. In §3, we present and discuss the main features of the flows, including the time-averaged flow structure, the power spectra and probability density distributions of a set of selected monitoring points, the turbulent statistics, the global kinetic energy balances and the internal waves motion phenomena. Both two- and three-dimensional sets of results are discussed and compared. Finally, relevant results are summarized and conclusions are given in §4.

2. Governing equations and numerical method

2.1. Governing equations

We consider a cavity of height L_3 , width L_2 and depth L_1 (height and depth aspect ratios are $A_3 = L_3/L_2$ and $A_1 = L_1/L_2$, respectively) filled with an incompressible Newtonian viscous fluid of kinematic viscosity ν and thermal diffusivity α . To account for the density variations, the Boussinesq approximation is used. Thermal radiation is neglected. Under these assumptions, the dimensionless governing equations in

primitive variables are

$$\left. \begin{aligned} \nabla \cdot \mathbf{u} &= 0, \\ \frac{\partial \mathbf{u}}{\partial t} + (\mathbf{u} \cdot \nabla) \mathbf{u} &= \frac{Pr}{Ra^{0.5}} \nabla^2 \mathbf{u} - \nabla p + \mathbf{f}, \\ \frac{\partial T}{\partial t} + (\mathbf{u} \cdot \nabla) T &= \frac{1}{Ra^{0.5}} \nabla^2 T, \end{aligned} \right\} \quad (2.1)$$

where Ra (here, for simplicity, the subindex 3 is dropped) is the Rayleigh number based on the cavity height $(g\beta\Delta TL_3^3)/(\nu\alpha)$ and $Pr = \nu/\alpha$ and the body force vector is $\mathbf{f} = (0, 0, PrT)$. The reference length, time, velocity, temperature and dynamic pressure used for the dimensionless form are, respectively, L_3 , $(L_3^2/\alpha)Ra^{-0.5}$, $(\alpha/L_3)Ra^{0.5}$, ΔT and $\rho(\alpha^2/L_3^2)Ra$. With the above reference quantities, the vertical buoyant velocity, $Pr^{0.5}$, and the characteristic dimensionless Brunt–Väisälä frequency, $N = (CPr)^{0.5}/(2\pi)$, where C is the dimensionless stratification of the time-averaged temperature field, are independent of the Rayleigh number.

The cavity is subjected to a temperature difference ΔT across the vertical isothermal walls ($T(x_1, 0, x_3) = 1$, $T(x_1, 1/A_3, x_3) = 0$) while the top and bottom walls are adiabatic. At the four planes $x_2 = 0$, $x_2 = 1/A_3$, $x_3 = 0$, $x_3 = 1$, non-slip boundary condition are imposed for velocity. Periodic boundary conditions in the x_1 -direction are used. The initial conditions are not relevant because the statistics of the flow are recorded after a long enough time-integration period to reach a statistically steady-state behaviour. Periodic vertical boundary conditions are used because they allow us to study the three-dimensional effects due to the intrinsic instability of the main flow and not to the boundary conditions. If we furthermore consider that the cavity is filled with air ($Pr = 0.71$) and that its height aspect ratio A_3 is equal to 4, then the configuration depends only on the Rayleigh number Ra and the depth aspect ratio A_1 .

2.2. Numerical method

2.2.1. Spatial discretization

Governing equations (2.1) are discretized on a staggered grid in space by second- and fourth-order spectro-consistent schemes by Verstappen & Veldman (1997, 1998, 2003). Following the same notation, the symmetry-preserving discretization of the Navier–Stokes equations becomes

$$\mathbf{M}\mathbf{u}_h = \mathbf{0}, \quad (2.2)$$

$$\mathbf{\Omega} \frac{d\mathbf{u}_h}{dt} = -\mathbf{C}(\mathbf{u}_h)\mathbf{u}_h + \mathbf{D}\mathbf{u}_h + \mathbf{f}_h - \mathbf{M}'\mathbf{p}_h, \quad (2.3)$$

where \mathbf{u}_h stands for the discrete velocity vector, $\mathbf{\Omega}$ is a positive-definite diagonal matrix representing the sizes of the control volumes, the convective coefficient matrix $\mathbf{C}(\mathbf{u}_h)$ is skew-symmetric, the discrete diffusive operator \mathbf{D} is a symmetric negative-definite matrix and \mathbf{M} is the discrete divergence operator. The discrete gradient operator is the transpose of the discrete divergence multiplied by a diagonal scaling $\mathbf{G} = -\mathbf{\Omega}^{-1}\mathbf{M}$. Such discretization preserves the underlying symmetry properties of the continuous differential operators. These global discrete operator properties ensure both stability and that the global kinetic-energy balance is exactly satisfied even for coarse meshes if incompressibility constraint is accomplished. Therefore, kinetic energy is not systematically damped by the discrete convective term or does not need to be damped explicitly to ensure the stability of the method. This is a crucial point because an artificial dissipation would interfere with the subtle balance between

Case	Ra	N_1	N_2	N_3	L_1	γ_2	γ_3	$(\Delta x_2)_{min}$	Δt	Total time	Average time	Order
A	6.4×10^8	128	156	312	2.0	1.5	1.5	2.44×10^{-4}	1.26×10^{-3}	1000	800	2
B	2×10^9	64	144	318	1.0	1.75	0.0	1.88×10^{-4}	1.27×10^{-3}	800	550	4
C	10^{10}	64	138	326	0.5	2.0	0.0	1.36×10^{-4}	1.49×10^{-3}	800	550	4
A2D	6.4×10^8	–	156	312	–	1.5	1.5	2.44×10^{-4}	1.40×10^{-3}	1000	800	2
B2D	2×10^9	–	144	318	–	1.75	0.0	1.88×10^{-4}	1.29×10^{-3}	800	550	4
C2D	10^{10}	–	138	326	–	2.0	0.0	1.36×10^{-4}	1.50×10^{-3}	800	550	4
AA2D	6.4×10^8	–	218	438	–	1.5	1.0	1.74×10^{-4}	6.96×10^{-4}	450	300	2
BB2D	2×10^9	–	202	448	–	1.75	0.0	1.33×10^{-4}	6.51×10^{-4}	325	200	4
CC2D	10^{10}	–	194	459	–	2.0	0.0	9.63×10^{-5}	7.56×10^{-4}	265	175	4
Xin & Le Quééré (1995)												
	6.4×10^8	–	64	128	–	–	–	1.51×10^{-4}	2.0×10^{-3}	400.0	–	–
	2×10^9	–	64	256	–	–	–	1.51×10^{-4}	1.5×10^{-3}	350.0	–	–
	10^{10}	–	96	768	–	–	–	6.69×10^{-5}	8.0×10^{-4}	250.0	150	–

TABLE 1. Physical and numerical simulation parameters.

convective transport and physical dissipation, especially at the smallest scales of motion. The energy transport equation is also discretized using a spectro-consistent scheme.

A second-order symmetry-preserving discretization was used for solving the lowest Ra number whereas the fourth-order counterpart has been used for the two highest (see table 1). Verstappen & Veldman (2003) showed that with the fourth-order method, coarser grids suffice to perform accurate numerical solutions. Therefore, here, grids with similar spatial resolution (see table 1) to those used in Soria *et al.* (2004) have been enough to solve cases with significantly higher Ra number.

2.2.2. Time-integration method

In order to simplify the notation, momentum equation (2.1) can be rewritten as

$$\frac{\partial \mathbf{u}}{\partial t} = \mathbf{R}(\mathbf{u}) - \nabla p, \quad (2.4)$$

where $\mathbf{R}(\mathbf{u})$ represents the right-hand side terms of the momentum equation except for the pressure gradient. For the temporal discretization, a central difference scheme is used for the time derivative term, a fully explicit second-order one-leg scheme proposed by Verstappen & Veldman (2003) for $\mathbf{R}(\mathbf{u})$ and a first-order backward Euler scheme for the pressure-gradient term. The incompressibility constraint is treated as implicit. Thus, we obtain the semi-discretized Navier–Stokes equations

$$\frac{(\beta + 1/2)\mathbf{u}^{n+1} - 2\beta\mathbf{u}^n + (\beta - 1/2)\mathbf{u}^{n-1}}{\Delta t} = \mathbf{R}((1 + \beta)\mathbf{u}^n - \beta\mathbf{u}^{n-1}) - \nabla p^{n+1}, \quad (2.5)$$

$$\nabla \cdot \mathbf{u}^{n+1} = 0, \quad (2.6)$$

where the parameter β is computed each time step to adapt the linear stability domain of the time-integration scheme to the instantaneous flow conditions in order to use the maximum Δt possible. Therefore, we look for stability domains which include eigenvalues $\lambda = x + iy$. As \mathbf{D} is a symmetric and negative-definite matrix, the real part x is negative and its values can be bounded by means of the Gershgorin circle

theorem. The skew-symmetry of the $\mathbf{C}(\mathbf{u}_h)$ discrete operator also allows us to bound the imaginary part y in the same way. Once eigenvalues are bounded, it is easy to compute the β value that better fits the linear stability domain. In all the DNS carried out here, the time step required for this dynamic scheme has been more than twice as great, that is twice cheaper, than the standard second-order Adams–Bashforth ($\beta = 1/2$) scheme. In practice, we choose the time step such that the time-integration becomes unstable when the selected time step is enlarged by 10 %.

To solve the velocity–pressure coupling, we use a classical fractional step projection method (see Chorin 1968; Yanenko 1971, for example). In the projection methods, solutions of the unsteady Navier–Stokes equations are obtained by first time-advancing the velocity field \mathbf{u} without regard for its solenoidality constraint (2.6), then recovering the proper solenoidal velocity field, \mathbf{u}^{n+1} ($\nabla \cdot \mathbf{u}^{n+1} = 0$). This projection is derived from the well-known Helmholtz–Hodge vector decomposition theorem (see Chorin 1993, for instance), whereby the velocity \mathbf{u}^{n+1} can be uniquely decomposed into a solenoidal vector, \mathbf{u}^p , and a curl-free vector, expressed as the gradient of a scalar field, $\nabla \tilde{p}$. This decomposition is written as

$$\mathbf{u}^p = \mathbf{u}^{n+1} + \nabla \tilde{p}, \quad (2.7)$$

where the predictor velocity \mathbf{u}^p is

$$\mathbf{u}^p = \frac{2\beta \mathbf{u}^n - (\beta - 1/2)\mathbf{u}^{n-1}}{\beta + 1/2} + \frac{\Delta t}{\beta + 1/2} \mathbf{R}((1 + \beta)\mathbf{u}^n - \beta \mathbf{u}^{n-1}), \quad (2.8)$$

and the pseudo-pressure is $\tilde{p} = \Delta t / (\beta + 1/2) p^{n+1}$. Taking the divergence of (2.7) yields a Poisson equation for \tilde{p}

$$\nabla \cdot \mathbf{u}^p = \nabla \cdot \mathbf{u}^{n+1} + \nabla \cdot (\nabla \tilde{p}) \longrightarrow \nabla^2 \tilde{p} = \nabla \cdot \mathbf{u}^p. \quad (2.9)$$

Once the solution is obtained, \mathbf{u}^{n+1} results from the correction

$$\mathbf{u}^{n+1} = \mathbf{u}^p - \nabla \tilde{p}. \quad (2.10)$$

2.2.3. Solution of the Poisson equation on a loosely coupled parallel computer

The discrete Laplacian operator of the Poisson equation (2.9) can be viewed as the product of the discrete divergence operator \mathbf{M} by the discrete gradient operator, which is the transpose of the discrete divergence multiplied by a diagonal scaling $\mathbf{G} = -\mathbf{\Omega}^{-1}\mathbf{M}$. So, the Laplacian operator is approximated by the matrix product $\mathbf{L} = -\mathbf{M}\mathbf{\Omega}^{-1}\mathbf{M}'$. Therefore the discrete Poisson equation to be solved at each time step is of the form

$$\mathbf{L} \mathbf{p}_h = \mathbf{M} \mathbf{u}_h^p. \quad (2.11)$$

Based on a domain decomposition strategy, the parallelization of the explicit parts of the code is straightforward. However, the efficient solution of the discrete Poisson equations is a critical aspect. This issue is specially relevant in a low cost PC cluster where the latency is high and the bandwidth network is low. Here, an extension to fourth-order schemes (see Trias *et al.* 2006*b*) of the original direct Schur–Fourier decomposition (DSFD) algorithm by Soria, Pérez-Segarra & Oliva (2003) is used. It is based on a combination of a direct Schur method (see Soria, Pérez-Segarra & Oliva 2002) in the two wall-normal directions and a Fourier decomposition in the periodic direction. This algorithm allows us to solve each three-dimensional Poisson equation to machine accuracy with only one all-to-all communication episode. This is

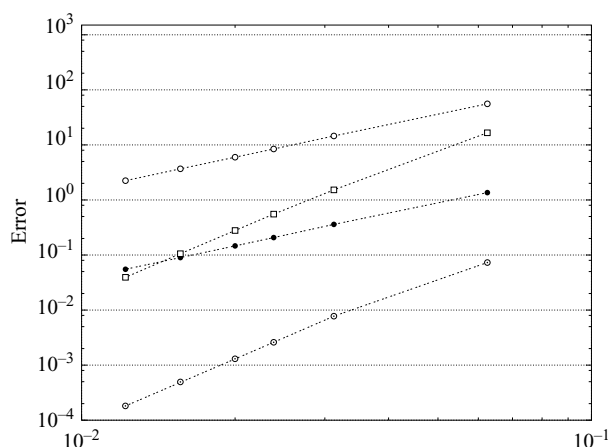


FIGURE 1. Numerical errors versus mesh size for convective (\circ , second-order; \square , fourth-order) and divergence (\bullet , second-order; \odot , fourth-order) operators for second- and fourth-order discretizations.

the crucial point that makes feasible the DNS of turbulent flows on loosely coupled parallel computers such as PC clusters.

2.3. Code and simulation verifications

2.3.1. Code verification

Before using the code developed for direct numerical simulations, it is necessary to verify that it is correct (i.e. that it solves the governing equations (2.1) with the prescribed boundary conditions and the expected order of accuracy). To do so, the method of manufactured solutions (MMS), described by Roache (2002), was used. In MMS, an arbitrary analytic function \mathbf{u}_a (that will be a solution of the PDE system and accomplish the incompressibility constraint) is chosen. Then, the source term \mathbf{f}_a that matches the arbitrary solution, is calculated analytically from the PDE system to be solved. The initial and boundary conditions are obtained evaluating \mathbf{u}_a . This procedure ensures that an analytic solution is obtained even for complex equations such as the Navier–Stokes system. This analytic source term \mathbf{f}_a is evaluated at the discretization nodes and used as input data for the numerical code. The time-dependent numerical solution \mathbf{u}_n is compared against \mathbf{u}_a , and it is checked that the orders of accuracy obtained are in good agreement with the theoretical ones (see figure 1). As the discretization is spectro-consistent, the exact fulfilment of the global kinetic energy balance (see § 3.4) has been for more details about the code verification see Soria *et al.* (2004).

2.3.2. Simulation verification

As no subgrid-scale model is used in the computation, the grid resolution and the time step must be sufficiently fine to solve all the relevant turbulence scales. Moreover, a sufficient length in the periodic direction is required to ensure that turbulence fluctuations are uncorrelated at a separation of a half-period. The time to begin the averaging period t_0 and the time integration period Δt_a must also be long enough to evaluate the flow statistics properly. Of course, for all these parameters, a compromise between accuracy and computing time must be accepted.

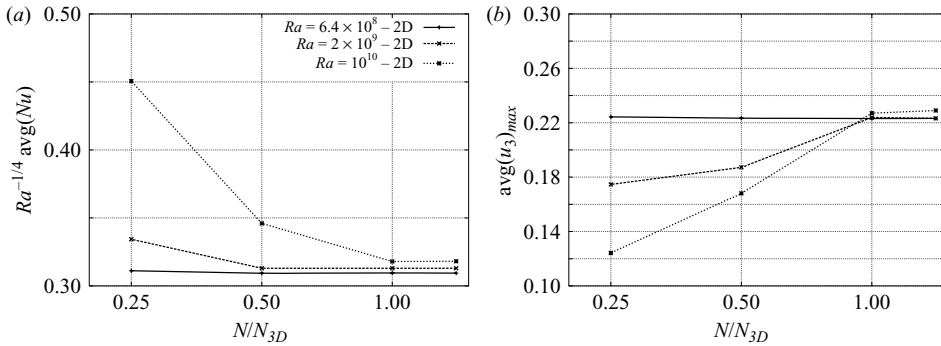


FIGURE 2. Examples of grid convergence study for two-dimensional simulations. (a) Overall averaged Nusselt number scaled by $Ra^{-1/4}$. (b) The maxima of $\overline{u_3}$ at the horizontal mid-height plane. The abscissa represents the ratio, on a logarithmic scale, of the number of nodes for each direction with respect to the number of nodes used for three-dimensional simulations (meshes A, B and C), i.e. $N_1/(N_1)_{3D} = N_2/(N_2)_{3D} = N_3/(N_3)_{3D} = N/N_{3D}$. Finest meshes correspond to two-dimensional cases AA2D, BB2D and CC2D (see table 1).

A total of 9 DNS have been carried out. The physical and numerical parameters for all cases are given in table 1. (N_1, N_2, N_3) are the number of grid points and γ_2 and γ_3 the concentration parameters (see (2.12)). Total time stands for the total integration time of Navier–Stokes equations from initial conditions (zero velocity field and uniformly distributed random temperatures between 0 and 1, in our case) and average time is the total time for computing statistics. In table 1, parameters of Xin & Le Quéré (1995) are also presented for comparison. Grid spacing in the periodic direction is uniform and the wall-normal points are distributed using a hyperbolic-tangent function

$$(x_2)_j = \frac{L_2}{2} \left(1 + \frac{\tanh\{\gamma_2(2(j-1)/N_2 - 1)\}}{\tanh \gamma_2} \right). \quad (2.12)$$

Spatial resolution in the two wall-normal directions is determined by means of a systematic procedure based on successive mesh refinements explained by Soria *et al.* (2004). Examples of the grid convergence studies for two-dimensional simulations are displayed in figure 2 where each of these points corresponds to one full simulation and statistical analysis. For the meshes corresponding to cases A, B and C ($N/N_{3D} = 1$), the results obtained seem to be reasonably close to the asymptotic value.

The mesh concentration factors γ_2 and γ_3 are computed to minimize the flow gradients on the computational space for a set of representative instantaneous maps. The increase of γ_2 arises because the boundary-layer thickness decreases with the Rayleigh number. Actually, the grid resolution near the isothermal vertical walls (see table 1) obtained with this computational method is in quite good agreement with the $Ra^{-1/4}$ laminar scaling. (The product $(\Delta x_2)_{\min} Ra^{1/4}$ takes values 3.88×10^{-2} , 3.97×10^{-2} and 4.31×10^{-2} for meshes corresponding to cases A, B and C, respectively.)

Finally, the direct comparison of our two-dimensional meshes (see table 1) and statistical results with those reported by Xin & Le Quéré (1995) reconfirms the adequacy of the grid resolution in the two wall-normal directions.

For three-dimensional simulations, the computational domain and grid resolution in the homogeneous direction must be adjusted to ensure that the turbulence fluctuations are uncorrelated at a separation of one half-period and the smallest relevant turbulent scales are also well-resolved. Two-point correlations and one-dimensional energy

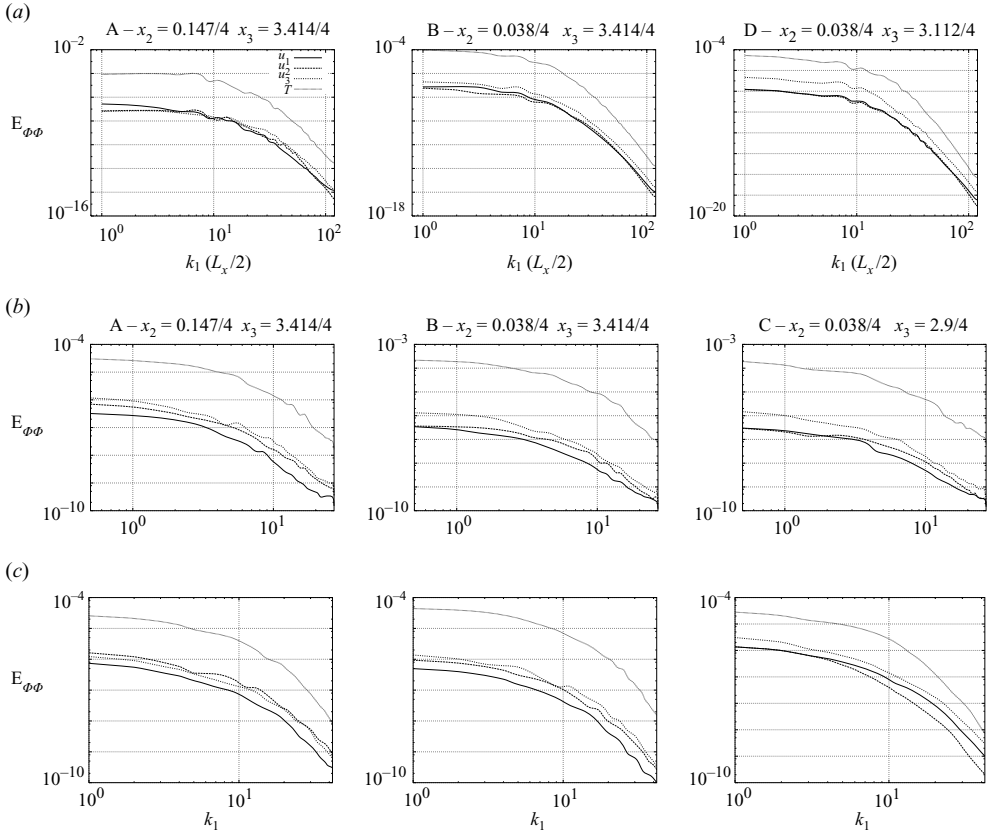


FIGURE 3. One-dimensional energy spectra at monitoring cavity locations at (a) $Ra = 6.4 \times 10^8$, (b) $Ra = 2 \times 10^9$ and (c) $Ra = 10^{10}$.

spectra defined, respectively, as,

$$R_{\phi\phi}(r_1, x_2, x_3) = \frac{\langle \phi'(x_1, x_2, x_3) \phi'(x_1 + r_1, x_2, x_3) \rangle}{\langle \phi'^2 \rangle}, \quad (2.13)$$

$$E_{\phi\phi}(k_1, x_2, x_3) = \langle \hat{\phi}_{k_1}(x_2, x_3) \hat{\phi}_{k_1}^*(x_2, x_3) \rangle, \quad (2.14)$$

where $(\cdot)^*$ and $\langle \cdot \rangle$ represent the complex conjugate and the average over time respectively, are shown in figures 3 and 4 to illustrate the adequacy of the computational domain and the grid resolution in the homogeneous direction. Three (x_2, x_3) -locations have been monitored for each case (see table 4). A detailed explanation of these locations is given in § 3.3.3.

Since there is no energy pile-up at high wavenumbers and the magnitude of the energy density between the smallest and the largest wavenumbers has dropped several orders of magnitude, the spanwise energy spectra displayed in figure 3 show that the grid resolutions are enough. Similar results are obtained for one-dimensional energy spectra computed at other (x_2, x_3) -locations.

In figure 4, spanwise two-point correlations $R_{\phi\phi}$ for the two wall-normal components of velocity and the temperature at the same monitoring points are shown. For the two lowest Ra numbers, the correlation values fall to zero for separations lower than one half-period showing that the computational domain in the spanwise direction

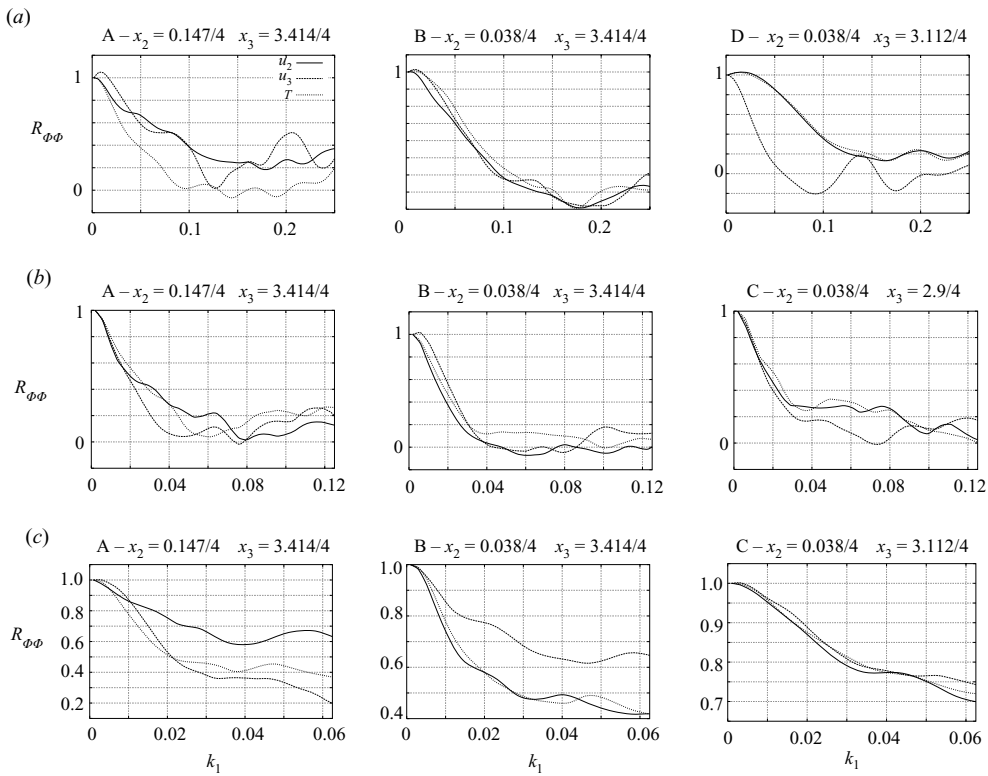


FIGURE 4. Two-point correlations at monitoring cavity locations at (a) $Ra = 6.4 \times 10^8$, (b) $Ra = 2 \times 10^9$ and (c) $Ra = 10^{10}$.

is sufficiently large. Soria *et al.* (2004) performed the three-dimensional simulation for the lowest Rayleigh number using the same spatial resolution in the spanwise direction, but with $L_1 = 1$. For such a configuration, two-point correlations $R_{\phi\phi}$ suggested that the computational domain was not large enough. Here, with $L_1 = 2$, uncorrelated turbulent fluctuations at a separation of half of the domain size are obtained. Nevertheless, when results are compared with those obtained with $L_1 = 1$, only insignificant differences are observed. Figure 4(c) shows that the two-point correlations $R_{\phi\phi}$ for the highest Rayleigh number at the centre of the cavity are significantly high. This indicates that the computational domain is not large enough but, based on the previous results at $Ra = 6.4 \times 10^8$, it is not thought to seriously affect any of the conclusions of the present work. Of course, future simulations with a larger domain size will be necessary to confirm this assertion.

3. Results and discussion

3.1. Time-averaged flow

Averages over the three statistically invariant transformations (time, x_1 -direction and central point symmetry around the centre of the cavity) are carried out for all fields. The time-averaged temperature fields and the streamlines of the averaged flow have been represented in the figure 5. A quantitative comparison with the results of Xin & Le Qu  r   (1995) is difficult, but (as expected), the two-dimensional results seem

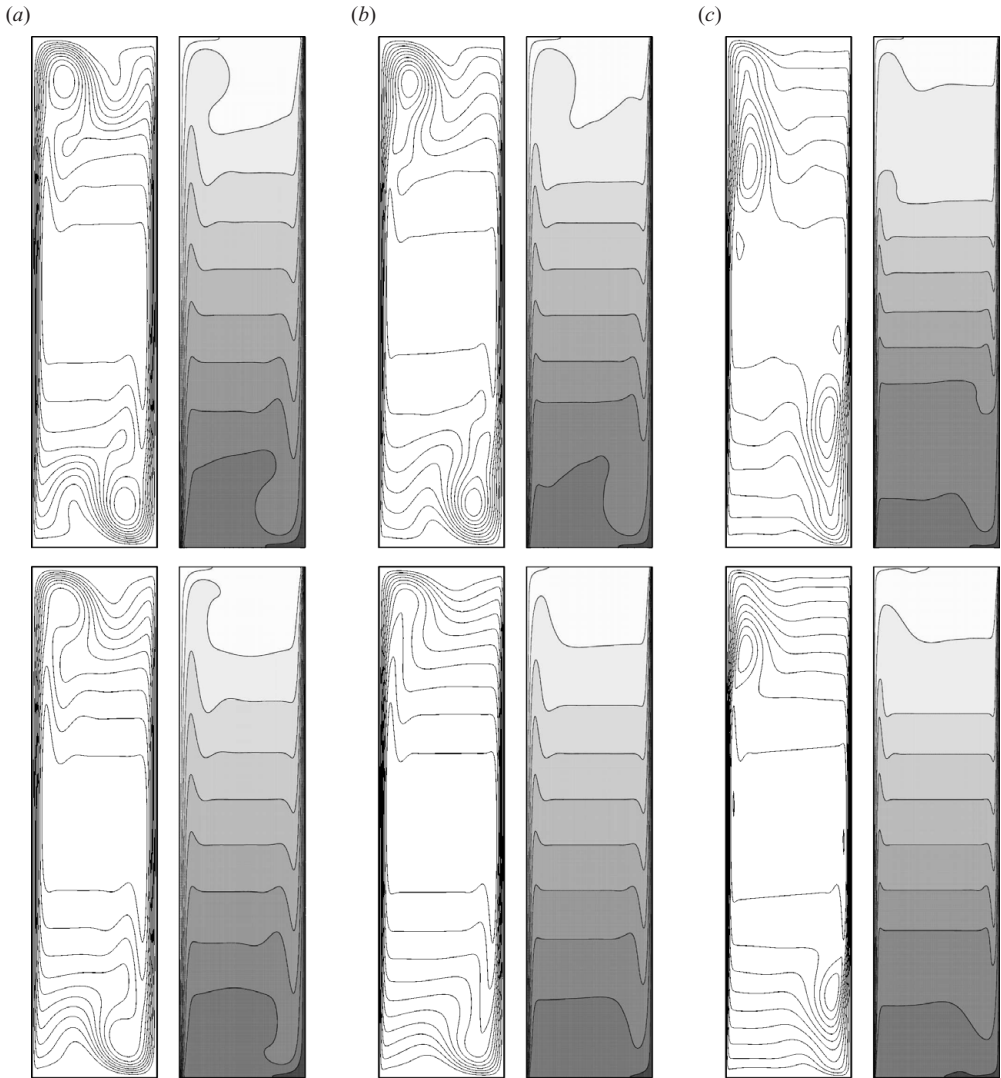


FIGURE 5. Averaged solutions: (a) $Ra = 6.4 \times 10^8$, (b) 2×10^9 and (c) 10^{10} . For each solution, the streamlines are on the left and temperature is on the right. For temperature fields, the isotherms are uniformly distributed from 0 to 1. Top: two-dimensional results. Bottom: three-dimensional results.

to be in very good agreement. A summary of several first-order statistics is presented in table 2 for direct comparison.

Despite the relatively large range of Rayleigh numbers, all them exhibit similar flow characteristics: thin vertical boundary layers and a large core area with very low time-averaged velocity and a stratified temperature distribution. When the two-dimensional and the three-dimensional results are directly compared we observe that the flow structure is still very similar for the first two Rayleigh numbers except for the formation of clearly stronger recirculations near the downstream corners (i.e. top left-hand and bottom right-hand corner.) for the two-dimensional simulations.

	AA2D	BB2D	CC2D	A	B	C
\overline{Nu}	49.23	66.19	100.60	49.24	66.63	101.70
\overline{Nu}_{max}	169.96	249.80	441.65	171.89	260.49	454.86
x_3	4.52×10^{-3}	1.12×10^{-3}	0	3.63×10^{-3}	0	0
\overline{u}_{2max}	8.69×10^{-4}	6.04×10^{-4}	6.18×10^{-4}	9.02×10^{-4}	6.36×10^{-4}	4.24×10^{-4}
x_2	2.22×10^{-1}	2.29×10^{-1}	5.26×10^{-3}	2.22×10^{-1}	2.29×10^{-1}	4.75×10^{-3}
\overline{u}_{3max}	2.23×10^{-1}	2.23×10^{-1}	2.29×10^{-1}	2.22×10^{-1}	2.22×10^{-1}	2.23×10^{-1}
x_2	7.51×10^{-3}	5.76×10^{-3}	3.75×10^{-3}	7.26×10^{-3}	5.76×10^{-3}	3.75×10^{-3}
$x_2 Ra^{1/4}$	4.78	4.87	4.74	4.62	4.87	4.74
\overline{u}_{2max}	2.32×10^{-2}	2.01×10^{-2}	8.30×10^{-3}	2.72×10^{-2}	1.76×10^{-2}	9.06×10^{-3}
x_3	9.49×10^{-1}	9.47×10^{-1}	9.58×10^{-1}	9.52×10^{-1}	9.57×10^{-1}	9.86×10^{-1}
\overline{u}_{3max}	4.49×10^{-2}	3.63×10^{-2}	2.60×10^{-3}	4.47×10^{-2}	1.67×10^{-2}	2.03×10^{-3}
x_3	8.41×10^{-2}	8.71×10^{-2}	2.31×10^{-1}	6.91×10^{-2}	6.01×10^{-2}	9.66×10^{-1}
\overline{T}_{max}	8.93×10^{-1}	8.90×10^{-1}	8.86×10^{-1}	8.91×10^{-1}	8.93×10^{-1}	9.07×10^{-1}
x_3	1	1	1	9.85×10^{-1}	1	1

TABLE 2. Summary of the averaged flow results. By rows, from top to bottom, the magnitudes are: the overall averaged Nusselt number, the maxima of the averaged local Nusselt and its position at the vertical hot wall, the maxima of \overline{u}_3 and \overline{T} at the horizontal mid-height plane and their respective x_2 positions, the maxima of \overline{u}_2 and \overline{T} at the vertical mid-width plane and their respective x_3 positions.

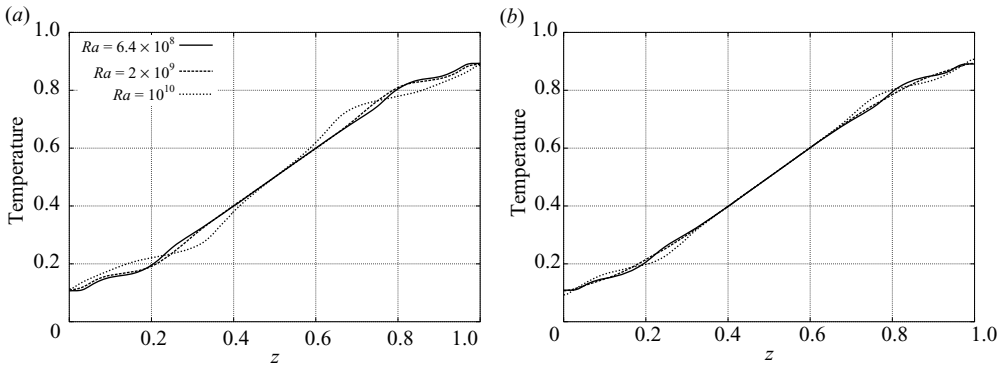


FIGURE 6. Averaged vertical temperature profile at mid-width. (a) Two-dimensional results. (b) Three-dimensional results.

The waves travelling downstream grow up to a point where they disrupt the boundary layers ejecting large unsteady eddies to the core of the cavity. The mixing effect of these eddies, that throw hot and cold fluid respectively, tends to result in almost isothermal hot upper and cold lower regions. The point where this phenomenon occurs moves upstream of the boundary layer when the Rayleigh number is increased. This mixing effect at the top and bottom areas of the cavity, clearly displayed in the time-averaged solutions (figures 5 and 6), forces the temperature drop in the core of the cavity to occur in a smaller region. The strengthening of the horizontal motion by means of large unsteady eddies also results in a remarkable thickening of the boundary layer in the downstream part and consequently a sudden decrease of the vertical velocity (figure 8) and a reduction of the wall-shear stress (figure 7).

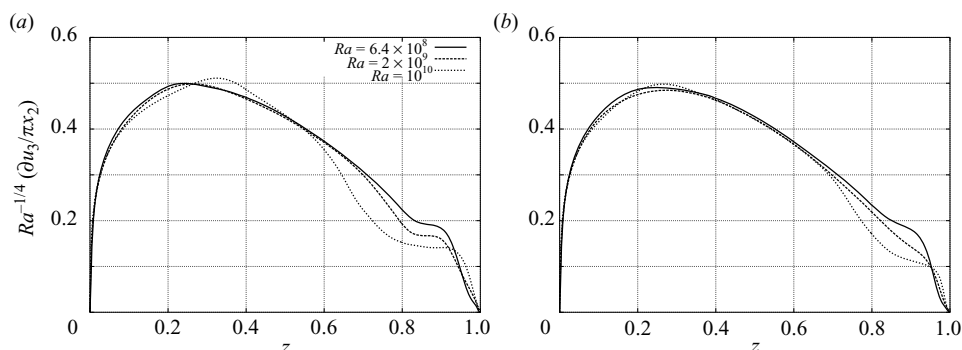


FIGURE 7. Dimensionless time-averaged wall shear stress scaled by $Ra^{-1/4}$. (a) Two-dimensional results. (b) Three-dimensional results.

However, when comparing two- and three-dimensional simulations, a weakening of all these effects is clearly observed in the three-dimensional results. Energy of the large eddies thrown from the boundary layers is rapidly driven to smaller scales by means of a vortex-stretching mechanism. As these large eddies do not persist in the three-dimensional simulations, the mixing effect is not so evident (figures 5 and 6) and the thickening of the boundary layer moves downstream (figure 8). A further explanation of these phenomena is given in §3.3.2.

The averaged temperature and vertical velocity component profiles displayed in figure 8, show that velocity maxima remain constant (see also table 2) and that identical profiles are obtained for more than half the vertical boundary layer when the lengths are scaled by the laminar $Ra^{1/4}$ factor. This laminar scaling is also observed in table 2 for the position of its maxima. Discrepancies occur only from the point where waves travelling downstream grow large enough to disrupt the boundary layer totally. These conclusions are exactly the same for both two- and three-dimensional simulations, confirming that in the range of Rayleigh numbers investigated, the main part of the vertical boundary layer is still laminar or quasi-laminar. This also confirms the adequacy of using the same grid resolution in the two wall-normal directions for both two-dimensional and three-dimensional configurations.

Thermal stratification in the core of the cavity is a basic questions that still remains open. Comparison between numerical and experimental results (see Salat *et al.* 2004, for a detailed overview) for a wide range of width/height aspect ratios give completely different results. Experimental studies yield a dimensionless stratification of about 0.5 whereas numerical simulations predict values about 1. According to the results obtained by Salat *et al.* (2004) and Soria *et al.* (2004), the two-dimensional assumption is not a critical issue in explaining these differences. Salat *et al.* (2004) also conclude that introducing experimental temperature measurements in the top and bottom wall instead of assuming the adiabaticity hypothesis do not improve the discrepancies in the thermal stratification. Our three-dimensional DNS results seem to confirm their conclusions with respect to the two-dimensional assumption. The only relevant difference observed (see table 5) is the slightly increased stratification value observed for the two-dimensional simulation of the largest Rayleigh number, also observed by Xin & Le Quéré (1995), that does not occur for the three-dimensional counterpart simulation. Thus, once two-dimensionality and the adiabaticity hypothesis have been discarded as critical issues, the next plausible candidates are the thermal

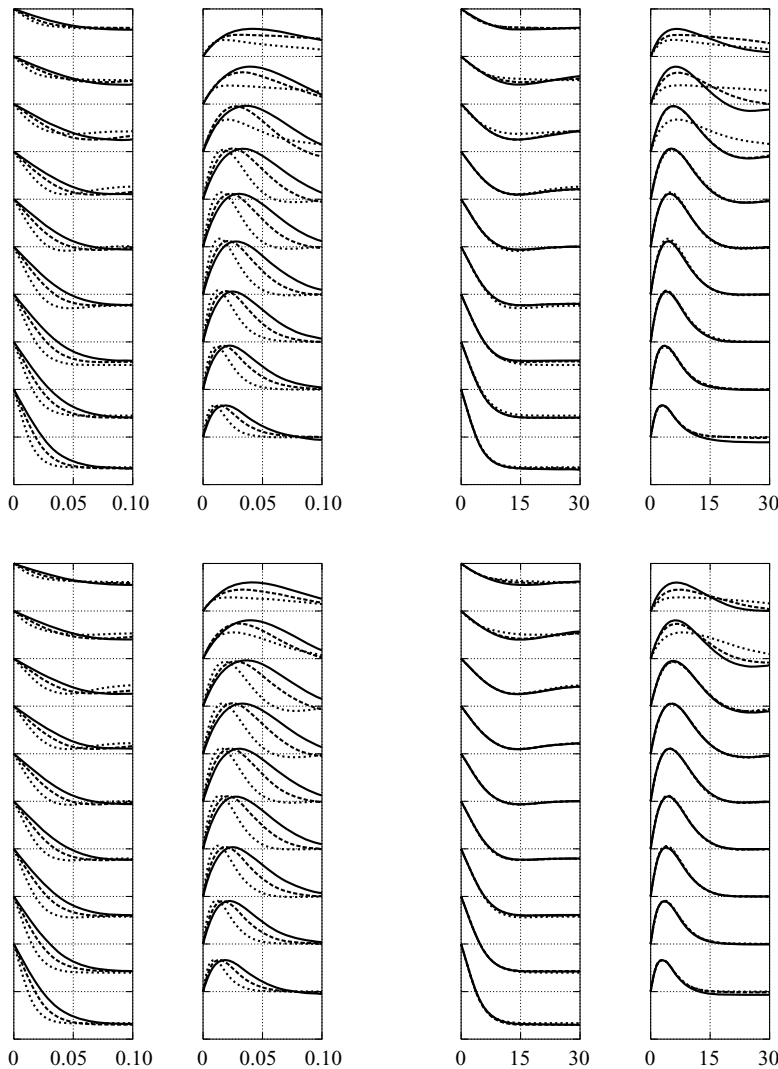


FIGURE 8. Averaged temperature (left-hand side of pair) and vertical velocity (right-hand side of pair) profiles at $z = 0.1, 0.2, 0.3, 0.4, 0.5, 0.6, 0.7, 0.8, 0.9$. Each vertical subdivision represents 0.5 units for temperature and 0.2 units for vertical velocity. For plots on the left, the abscissa scale factor is $4x_2$ and for plots on the right, is $4x_2Ra^{1/4}$. Top: two-dimensional results. Bottom: three-dimensional results. Ra values as figure 7.

radiation effects, the isothermal hypothesis of the vertical walls and the Boussinesq approximation.

3.2. Heat transfer

As expected from the similarity between the two-dimensional and three-dimensional averaged thermal boundary layers, the time-averaged and spatial mean Nusselt numbers are almost equal (see table 3) although slightly higher values are obtained for three-dimensional results. (The reference heat flux is given by $\lambda\Delta T/L_3$, where λ is the thermal conductivity. Thus, the dimensionless local Nusselt number at the vertical hot wall is given by $Nu = -\partial T/\partial x_2|_{x_2=0}$.) Table 3 also shows that Nusselt number correlation is much closer to the $Ra^{1/4}$ correlation for laminar flow than the $Ra^{1/3}$

Case	Ra	\overline{Nu}	\overline{Nu}_{x_Q}	$\overline{Nu}/Ra^{1/4}$	$\overline{Nu}/Ra^{1/3}$	\overline{Nu}_{down}	$\overline{Nu}_{down}/Ra^{1/3}$
AA2D	6.4×10^8	49.23	49.2	0.3095	0.05712	3.00	3.48×10^{-3}
BB2D	2×10^9	66.19	66.5	0.3129	0.05253	4.48	3.56×10^{-3}
CC2D	10^{10}	100.60	101.0	0.3181	0.04669	7.01	3.25×10^{-3}
A	6.4×10^8	49.24	–	0.3096	0.05713	2.98	3.45×10^{-3}
B	2×10^9	66.63	–	0.3151	0.05288	4.54	3.60×10^{-3}
C	10^{10}	101.70	–	0.3216	0.04720	7.86	3.65×10^{-3}

TABLE 3. Nusselt number and correlations.

correlation for turbulent flow. The reason for such behaviour is that most of the heat transfer occurs in the upstream part of the boundary layer where it is almost laminar. To confirm this point, we have computed the mean Nusselt number at the most downstream part where the boundary layer becomes turbulent. In the last column of table 3, we see that the \overline{Nu}_{down} , that has been integrated from $x_3 = 0.8$ to $x_3 = 1$ over the hot sidewall, is very close to the classical $Ra^{1/3}$ turbulent scaling. This confirms that at the most downstream part, boundary layers become turbulent.

The averaged local Nusselt distributions are also very similar, as can be observed in the figure 9 (left-hand side). However, there are significant differences in the standard deviation of the local Nusselt numbers. As can be observed in figure 9 (right-hand side), large fluctuations, which always occur in the downstream part of the boundary layer whereas upstream is almost laminar, display evident differences between two- and three-dimensional configurations. For two-dimensional simulations, this region of large fluctuations increases with the Rayleigh number and the standard deviation maxima position moves downstream of the boundary layer. These phenomena has also been observed by Xin & Le Quéré (1995) in their two-dimensional simulations. However, for the three-dimensional simulations this region seems to remain almost invariant slightly above $x_3 = 0.6$ position while the peak moves upstream. Standard deviation maxima display similar values to the two-dimensional counterpart, but occur at higher positions. Another important difference is observed in the almost laminar upstream part, where both profiles seem to collapse when the Rayleigh number is increased.

3.3. Flow dynamics

A general view of the several instantaneous temperature fields is displayed in figure 10. At first sight, we can see that when the Ra number is increased, important differences between two- and three-dimensional simulations are observed. With the aim of elucidating the origin of such differences and the physical mechanisms involved, several flow dynamics aspects are analysed and discussed in the next sections.

3.3.1. Two- and three-dimensional turbulence

As is well known, the most relevant feature of ‘two-dimensional turbulence’ is its ability to form large persistent vortices even out of an initially disordered flow, by means of an inverse cascade of energy. This self-organization of two-dimensional flows can be explained by considering the convective contribution to the temporal evolution of the enstrophy

$$\frac{1}{2} \frac{d}{dt} \int_{\Omega} \mathbf{w}^2 d\Omega = -\frac{Pr}{Ra^{0.5}} \int_{\Omega} (\nabla^2 \mathbf{u})^2 d\Omega + \int_{\Omega} ((\mathbf{u} \cdot \nabla) \mathbf{u}) \cdot \nabla^2 \mathbf{u} d\Omega - \int_{\Omega} \mathbf{f} \cdot \nabla^2 \mathbf{u} d\Omega, \quad (3.1)$$

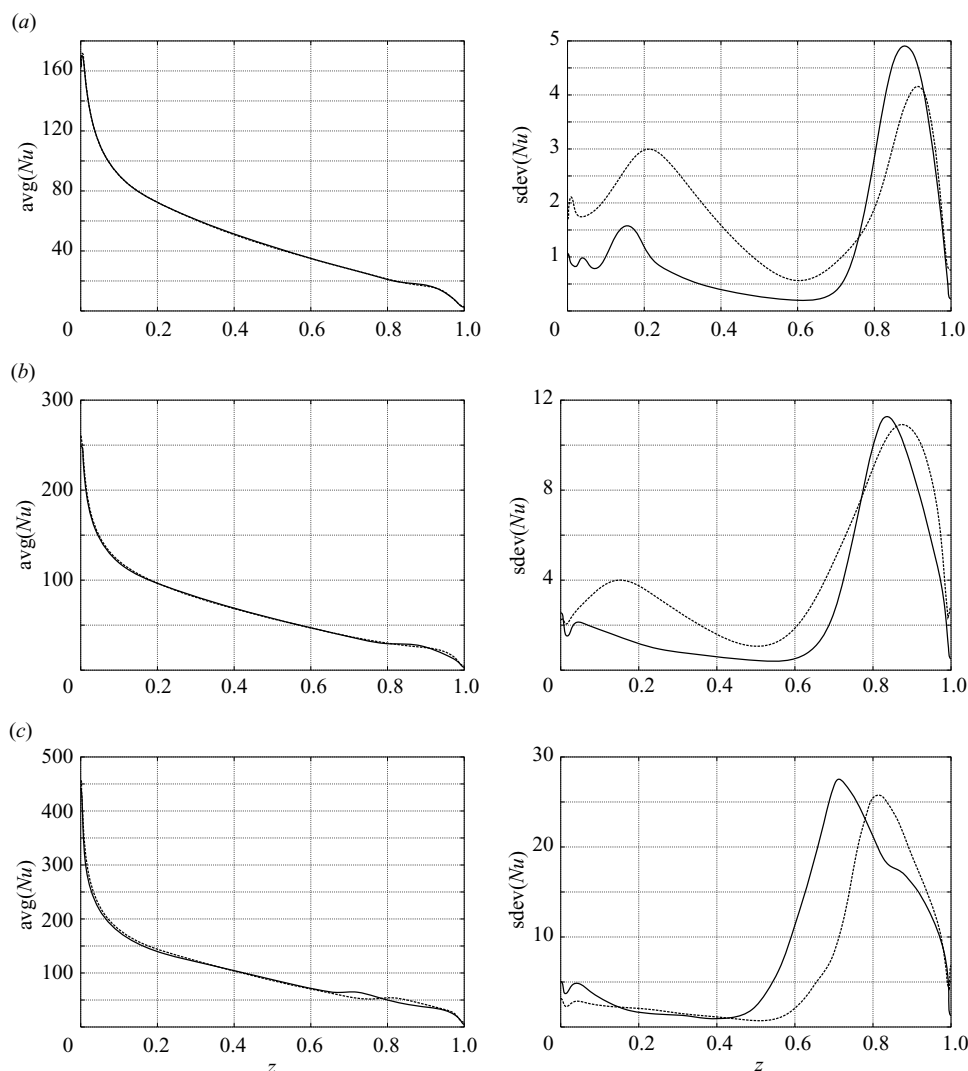


FIGURE 9. Local Nusselt number distribution (left-hand side) and their standard deviation (right-hand side): (a) $Ra = 6.4 \times 10^8$, (b) $Ra = 2 \times 10^9$ and (c) $Ra = 10^{10}$. Solid line, two-dimensional; broken line, three-dimensional.

where $\mathbf{w} = \nabla \times \mathbf{u}$ is the vorticity. When the flow is forced to be two-dimensional, the convective term becomes zero,

$$\int_{\Omega} ((\mathbf{u} \cdot \nabla) \mathbf{u}) \cdot \nabla^2 \mathbf{u} \, d\Omega = 0, \quad (3.2)$$

for any incompressible velocity field (if the boundary terms vanish, as in our configuration). This additional enstrophy invariant for two-dimensional Navier–Stokes equations, when viscosity and forcing terms are ignored, is responsible for the characteristic inverse energy cascade (see the pioneering work of Kraichnan 1967, for instance). In three dimensions, the convective contribution does not vanish and the energy is driven to smaller scales of motion by means of the vortex-stretching mechanism.

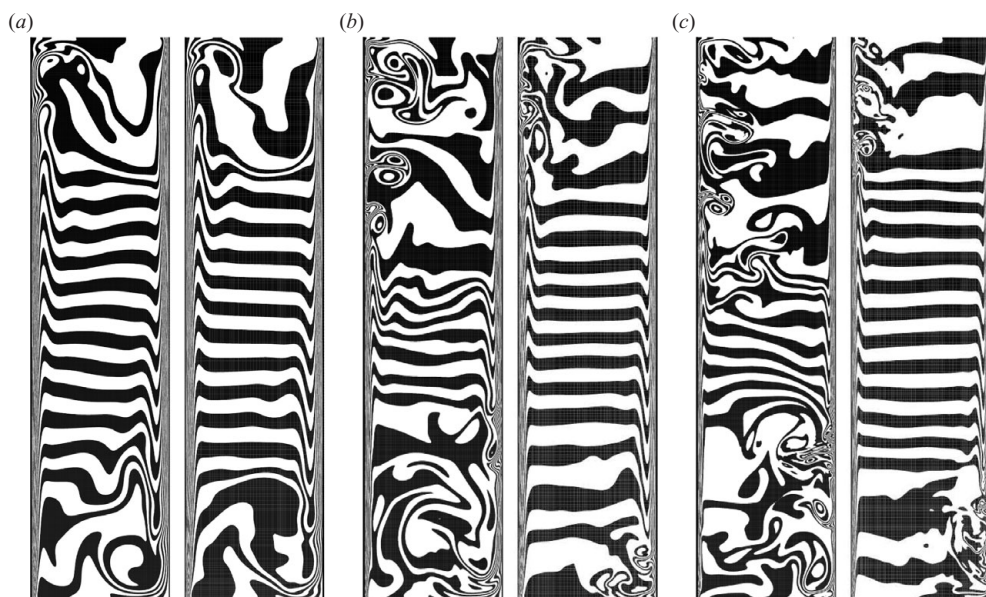


FIGURE 10. Instantaneous isotherms: (a) $Ra = 6.4 \times 10^8$, (b) 2×10^9 and (c) 10^{10} . For each solution the two-dimensional results are on the left and the three-dimensional results on the right. The isotherms are uniformly distributed from 0 to 1.

In our case, despite the relatively low Rayleigh numbers considered, significant differences between two-dimensional and three-dimensional turbulence flow dynamics are observed in the time sequences of the two-dimensional sections of isotherms displayed in figures 12 and 13. Two-dimensional animations show persistent vortices that are transported to the centre of the cavity. This phenomenon becomes more marked for the two highest Rayleigh numbers.

These features of the two- and three-dimensional flows are also important from a theoretical point of view. The orthogonality property (3.2) is widely used in the proof of existence and uniqueness of weak and strong solutions of the two-dimensional Navier–Stokes equations. However, in three dimensions, this is still an open problem. Verstappen (2007) and Trias *et al.* (2006a) note the importance of preserving the symmetry properties that form the basis for the conservation of kinetic energy, enstrophy (in two dimensions) and helicity (in three dimensions) in regularization modelling of turbulence. Note that, as discussed in §2.2.1, the spatial discretization used here preserves the underlying symmetries of the continuous differential operators and therefore it holds discretely all these global inviscid invariants.

3.3.2. Instantaneous fields

Figures 11, 12 and 13 show time sequences of instantaneous temperature fields. Soria *et al.* (2004) analysed in detail the dynamics of the lowest Rayleigh number considered here and concluded that both two- and three-dimensional configurations have a motionless and stratified cavity core and concentrate important fluctuations in the two downstream corners of the cavity. The main differences occur in the vertical boundary layers. For the two-dimensional simulation, it is almost totally stable and only periodic oscillations can be observed in the most downstream part of the boundary layer whereas in the three-dimensional simulation, instabilities generated in the upstream corner move downstream resulting in high values for turbulent statistics

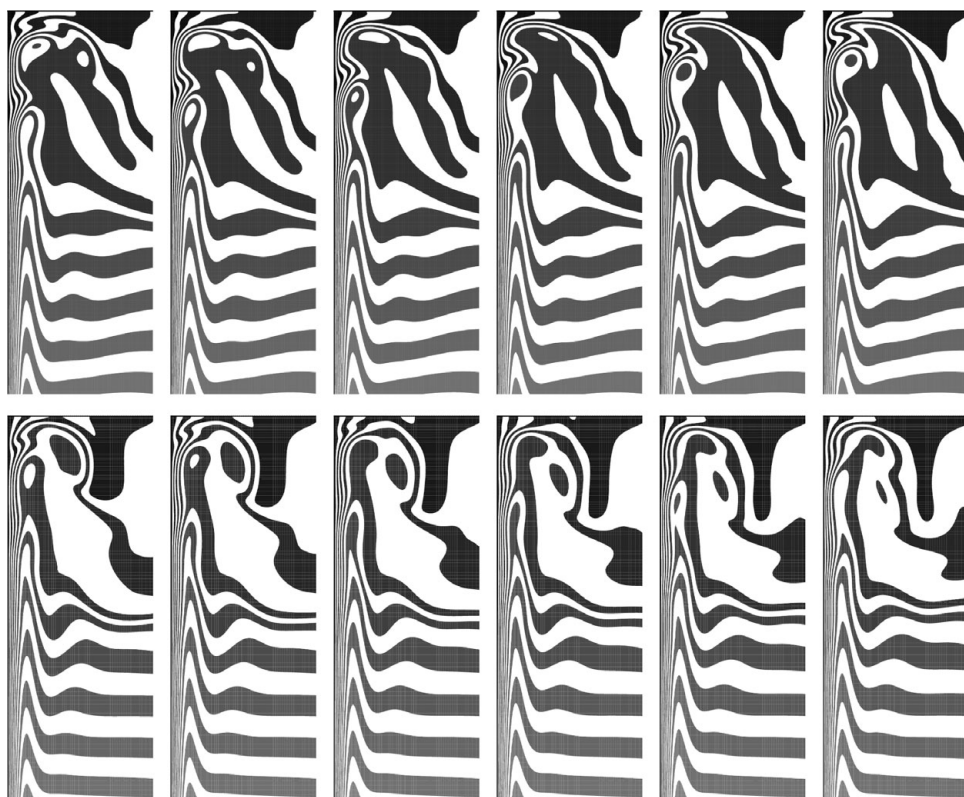


FIGURE 11. Time sequence of instantaneous isotherms at $Ra = 6.4 \times 10^8$. Zoom around the top left-hand corner. Time step between consecutive snapshots is ≈ 0.25 . Top: two-dimensional simulation. Bottom: three-dimensional simulation. The isotherms follow the same uniform distribution as used in figure 10.

at the vertical boundary layer, as discussed in following sections. Also, in the two-dimensional results, the vortices at the end of the vertical boundary layers are more vigorous and stable, as can also be appreciated in the streamline maps displayed in figure 5 (left-hand sides). Occasionally, in the three-dimensional simulation, there are large instability episodes where the three-dimensional structures generated at the top right-hand and bottom left-hand areas of the cavity propagate across all the vertical boundary layers. However, this phenomenon (that has not been observed in the two-dimensional results) is too infrequent to generate significant values of $\overline{u'_1 u'_1}$ and $\overline{u'_2 u'_2}$ at the vertical boundary layers.

At $Ra = 2 \times 10^9$, for the two-dimensional simulation, the oscillations at the downstream of the boundary layer are clearly stronger ejecting large eddies into the cavity core where the isotherms exhibit a periodical motion around the mean horizontal position. Such two-dimensional large-scale coherent vortex structures are very effective in convective transport. However, in the three-dimensional simulation these large eddies do not persist and their energy is rapidly passed down the cascade to smaller eddies. It yields a manifest reduction of the large-scale mixing effect at the hot upper and cold lower regions and consequently a still motionless stratified cavity core.

For the highest Rayleigh number, $Ra = 10^{10}$, differences between the two- and three-dimensional simulations become more marked. The boundary layers still remain laminar in their upstream part up to the point where large unsteady eddies are ejected

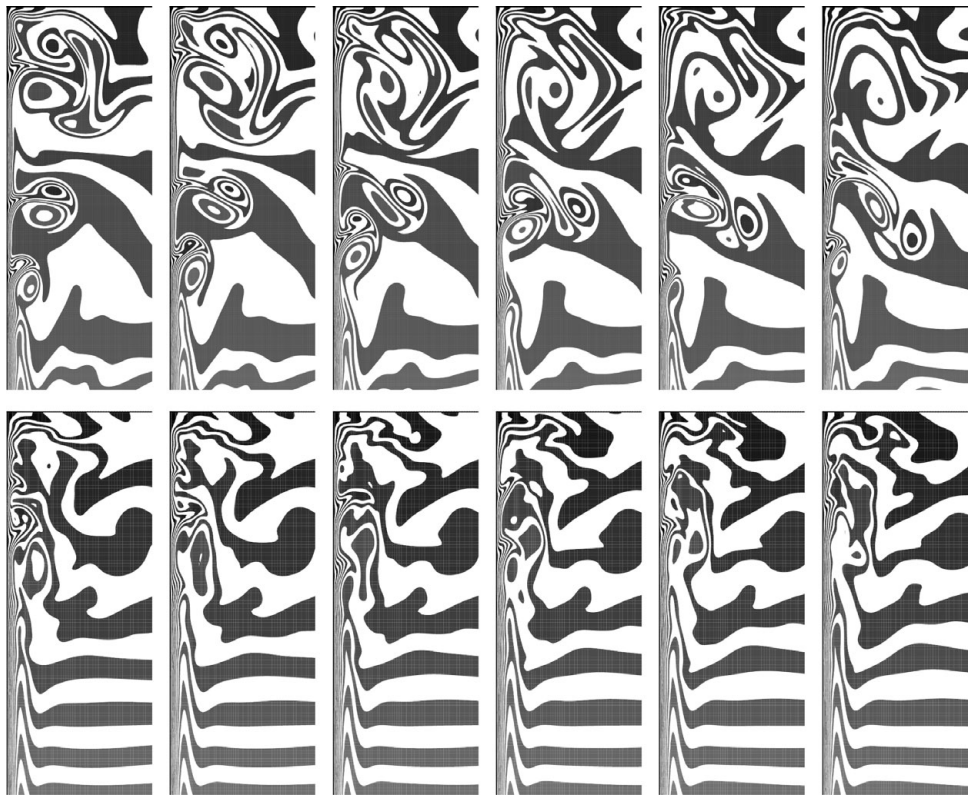


FIGURE 12. As figure 11, but for $Ra = 2 \times 10^9$ and time step ≈ 0.335 .

Point	x_2	x_3	6.4×10^8	2×10^9	10^{10}
A	0.03675	0.8535	×	×	×
B	0.0095	0.8535	×	×	×
C	0.0095	0.725		×	
D	0.0095	0.778	×		×

TABLE 4. Monitoring cavity locations.

into the cavity core. For the two-dimensional simulation, this occurs around $x_3 = 0.6$ (at the hot vertical wall) which agrees well with Xin & Le Quéré (1995), meanwhile for the three-dimensional one, the vertical boundary layer remains laminar up to $x_3 = 0.75$. This was also observed when comparing time-averaged profiles with lengths scaled by a $Ra^{1/4}$ factor in figure 8 (right-hand sides). At this Rayleigh number, again large vortices ejected from the boundary layer are rapidly stretched and the mixing effect clearly reduced. The cavity core remains almost motionless and well stratified, in an evident contrast with the two-dimensional simulation results that display increasingly large top and bottom regions of disorganization that consequently reduce the area of uniform temperature stratification.

3.3.3. Power spectra and probability density functions

Time traces of the temperature and the two wall-normal velocity components have been monitored at the same points as used by Xin & Le Quéré (1995) (see table 4)



FIGURE 13. As figure 11, but for $Ra = 10^{10}$. Time step ≈ 0.281 .

for a direct comparison. These points are located in the downstream part of the hot boundary layer. Points B, C and D are located around the maximum velocity while A is located at the outer edge of the boundary layer.

The probability density functions (PDF) of the temperature and velocity signals for the two highest Rayleigh numbers at the monitored positions are displayed in figures 14 and 15. The results are in a good agreement with the two-dimensional results of Xin & Le Quéré (1995). Wall effects and stratification of the core of the cavity are sources of the anisotropy seen in the PDF of the u_2 velocity component for which the proximity of the wall prevents large negative fluctuations while positive ones are not constrained. At $Ra = 2 \times 10^9$, the effect of three-dimensional fluctuations produces slightly different PDF profiles, specially for the vertical velocity component. For the highest Rayleigh number, the three-dimensional results display a significantly higher range of values for the u_2 component of velocity. However, as expected, the most evident differences between two- and three-dimensional results occur at the point labelled A, located at the outer edge of an already disrupted boundary layer. As we have seen in § 3.3.2, such disruption occurs at a more downstream location for the three-dimensional simulations and this difference become more marked when the Ra number is increased.

Normalized density power spectra of temperature displayed in figures 16 and 17 show that low-frequency modes contain a large part of the total energy. (The power spectrum of each variable is normalized such that the peak be equal to unity.) Only for $Ra = 2 \times 10^9$ simulations and for the three-dimensional simulation of the highest

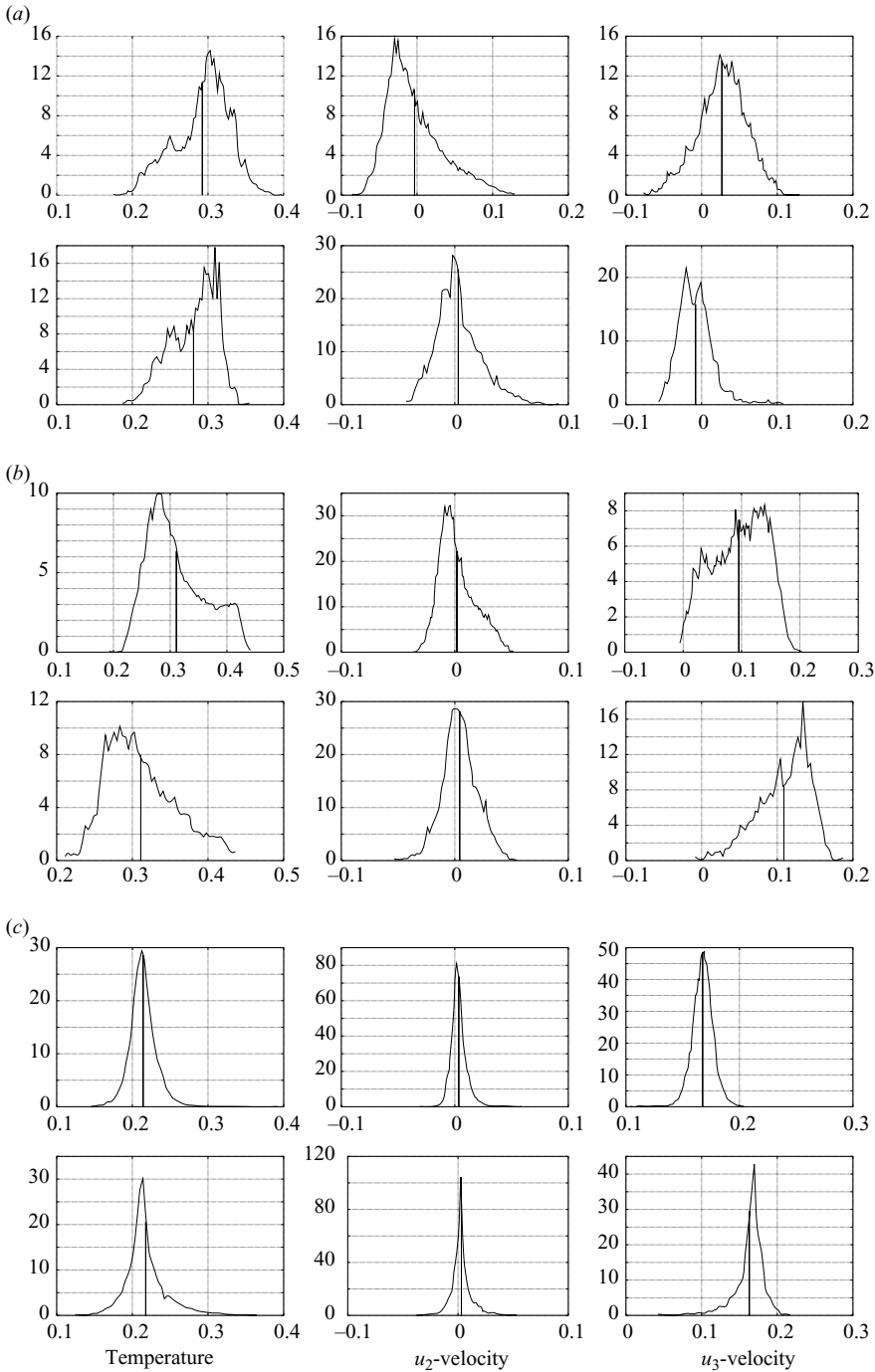


FIGURE 14. Probability density functions at (a) A, (b) B and (c) C for $Ra = 2 \times 10^9$. Vertical lines indicate the time-averaged values. Top: two-dimensional results. Bottom: three-dimensional results.

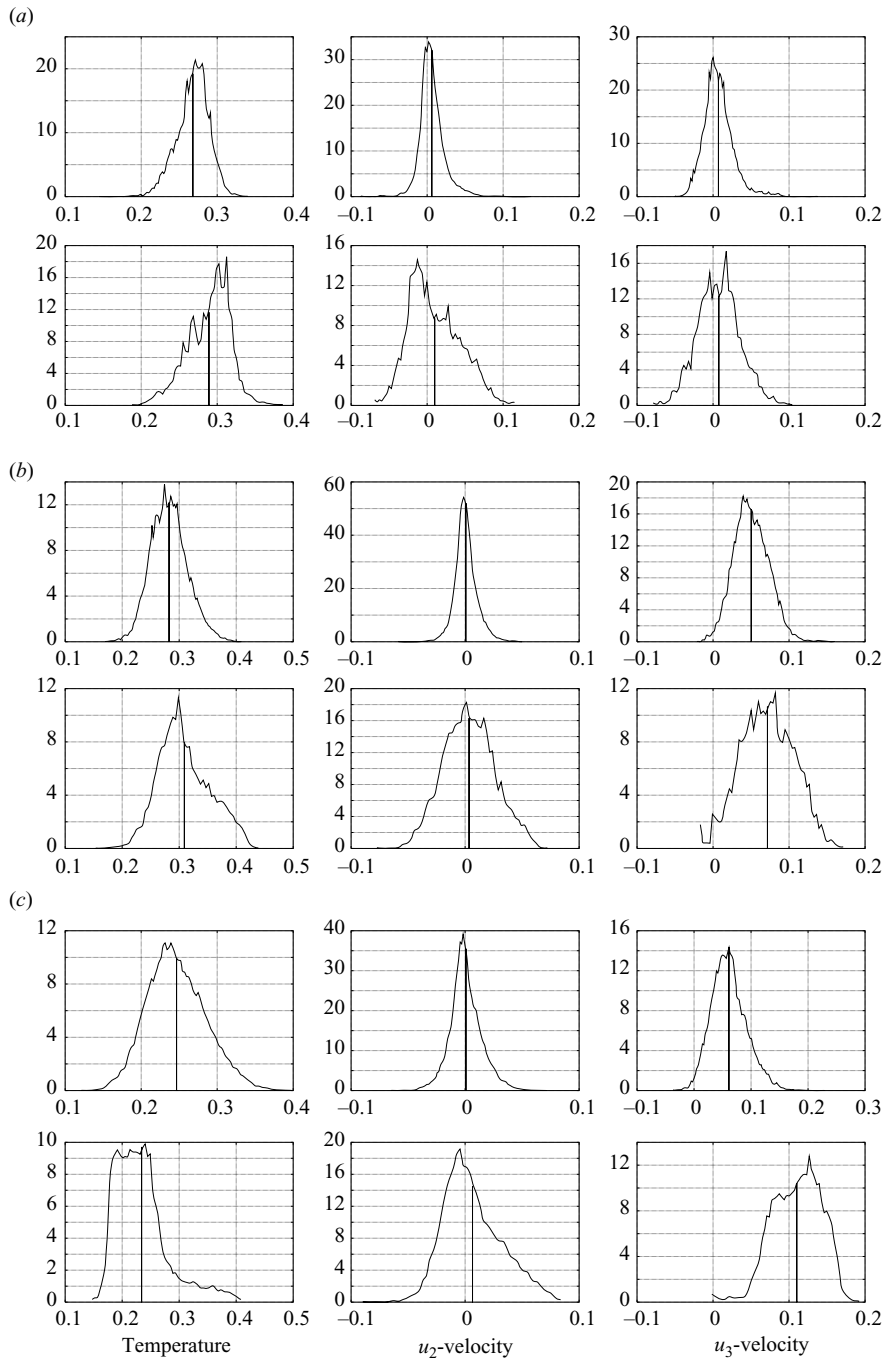


FIGURE 15. Probability density functions at (a) A, (b) B and (c) D for $Ra = 10^{10}$. Vertical lines indicate the time-averaged values. Top: two-dimensional results. Bottom: three-dimensional results.

Rayleigh number and at the lowest location C, the high-frequency boundary-layer instability becomes clearly evident. This high-frequency mode is still slightly visible at point B, specially for the three-dimensional simulations, whereas at point A, that

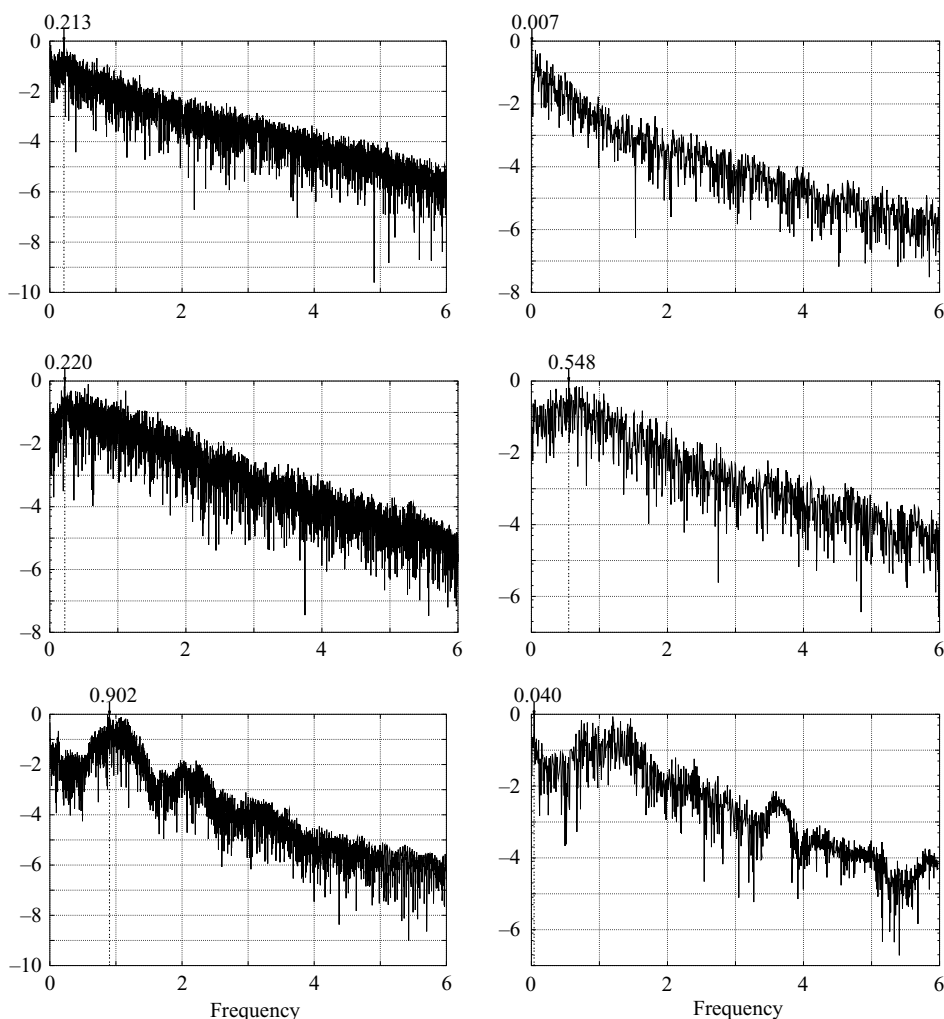


FIGURE 16. Normalized density power spectra of temperature. From top to bottom: at A, B and C for $Ra = 2 \times 10^9$. Left-hand side: two-dimensional results. Right-hand side: three-dimensional results.

it is almost at the cavity core, the power spectra is dominated by very low-frequency oscillations. The origin of such oscillations is related to the formation of the large unsteady eddies ejected from the most downstream part of the boundary layer into the cavity core. This explains the persistence of the high frequency of the boundary-layer instability for the three-dimensional simulations at the B and C locations, whereas for the two-dimensional simulations the boundary layers have already been totally disrupted.

3.3.4. Internal waves

Although the velocities in the core of the cavity become much smaller compared to the velocities in the vertical boundary layers for increasing Rayleigh number (see figure 8), simulations show that the cavity core is in motion and the isotherms in this region oscillate around the mean horizontal profile. Since the core of the cavity

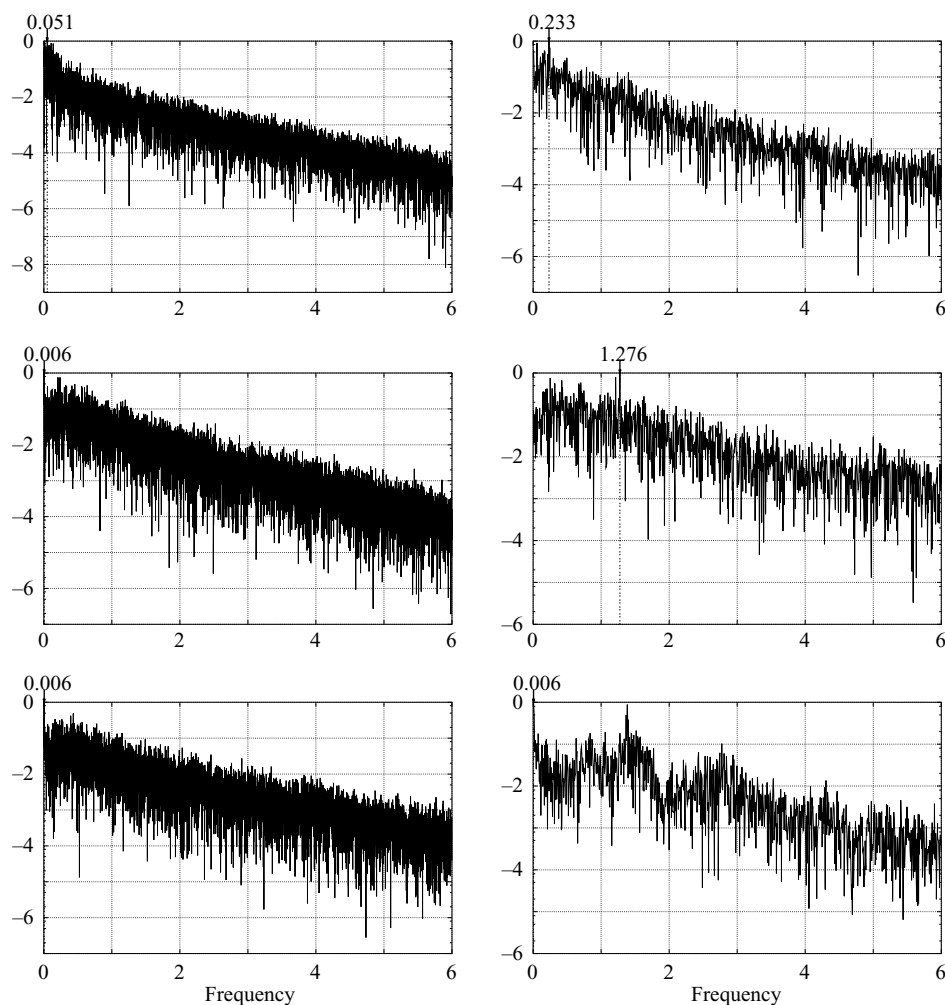


FIGURE 17. Normalized density power spectra of temperature. From top to bottom: at A, B and D for $Ra = 10^{10}$. Left-hand side: two-dimensional results. Right-hand side: three-dimensional results.

is well stratified (see figures 5 and 6), this phenomenon can probably be attributed to internal waves. Traditionally, the mean Nusselt number through the vertical mid-plane Nu_c has been used to characterize this wave motion. The normalized density power spectra of Nu_c (figure 18) show that fundamental frequencies for two- and three-dimensional simulations are similar. Since stratification of the time-averaged temperature fields in the core region is not significantly influenced by the three-dimensional fluctuations, we could expect such agreement. However, it was not clear *a priori* that excitation frequencies that characterize the largest structures in the three-dimensional configurations were large enough to excite the internal wave motion permanently. In table 5, these fundamental oscillation frequencies are compared with the dimensionless Brunt–Väisälä frequencies: $N = (CPr)^{0.5}/(2\pi)$ (see Lighthill 2002, for instance), where C is the dimensionless stratification of the time-averaged temperature. The results show a relatively good agreement between both sets of values for all configurations.

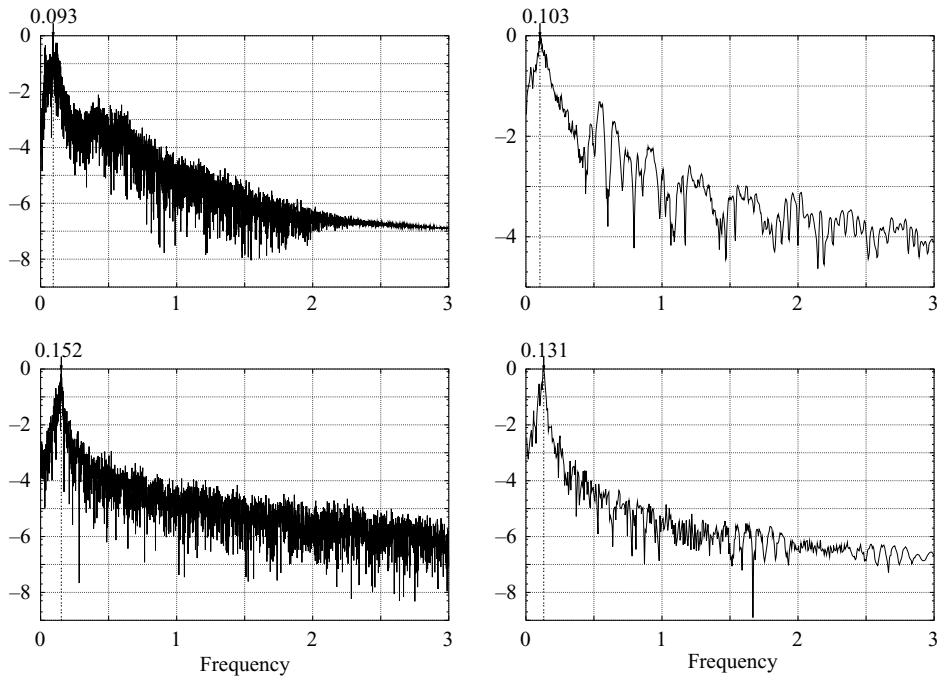


FIGURE 18. Normalized density power spectra of Nusselt number at the vertical mid-plane. From top to bottom: $Ra=2 \times 10^9$ and $Ra=10^{10}$. Left-hand side: two-dimensional results. Right-hand side: three-dimensional results.

Ra	2D	3D	Xin & Le Quéré	C_{2D}	C_{3D}	C_{XQ}	$(N)_{2D}$	$(N)_{3D}$	$(N)_{XQ}$
6.4×10^8	0.093	0.103	—	1.01	1.02	—	0.135	0.135	—
2×10^9	0.128	—	0.130	1.00	1.01	1.00	0.134	0.135	0.134
10^{10}	0.152	0.131	0.137	1.08	1.02	1.20	0.140	0.135	0.147

TABLE 5. From left to right: fundamental frequencies of the Nu_c , dimensionless stratification in the core of the cavity and Brunt–Väisälä frequency.

The dispersion relation for a linearly stratified fluid is given by $\omega^2 = N^2/(1+m^2/k^2)$, where ω is the excitation frequency and k and m are the horizontal and vertical components of the wave vector generated (see Lighthill 2002, for example). Moreover, the angle between the excitation and the propagation wavenumbers is given by $\theta = \arccos(\omega/N)$. Thus, internal waves are generated only if $\omega \leq N$. When the system is excited at the eigenfrequency ($\omega = N$), wave propagation is in the same direction as excitation whereas low excitation frequencies ($\omega \ll N$) generate perpendicular wave propagations. Therefore, as was pointed out by Xin & Le Quéré (1995), the permanent excitation of internal waves is due to the large eddies ejected from the vertical boundary layer at the hot upper and cold lower regions. We conclude that these eddies are large enough, even in the three-dimensional configurations, to be characterized by excitation frequencies ω smaller than the Brunt–Väisälä frequency and therefore permanently maintain an internal wave motion.

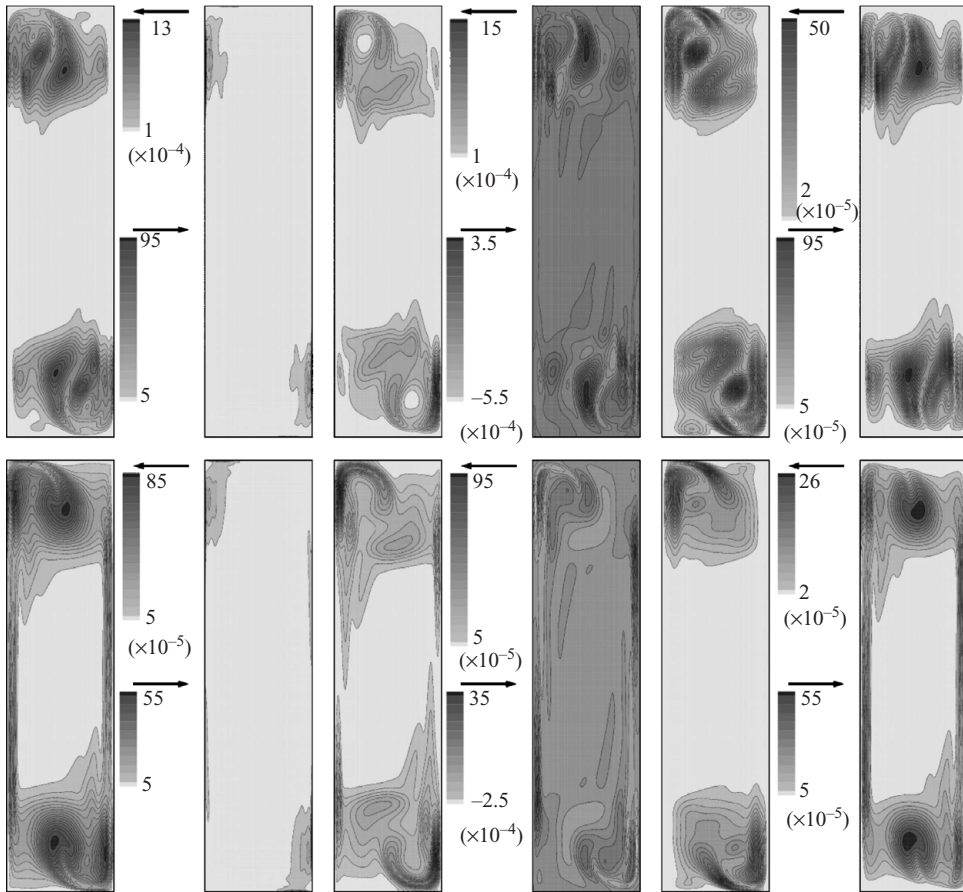
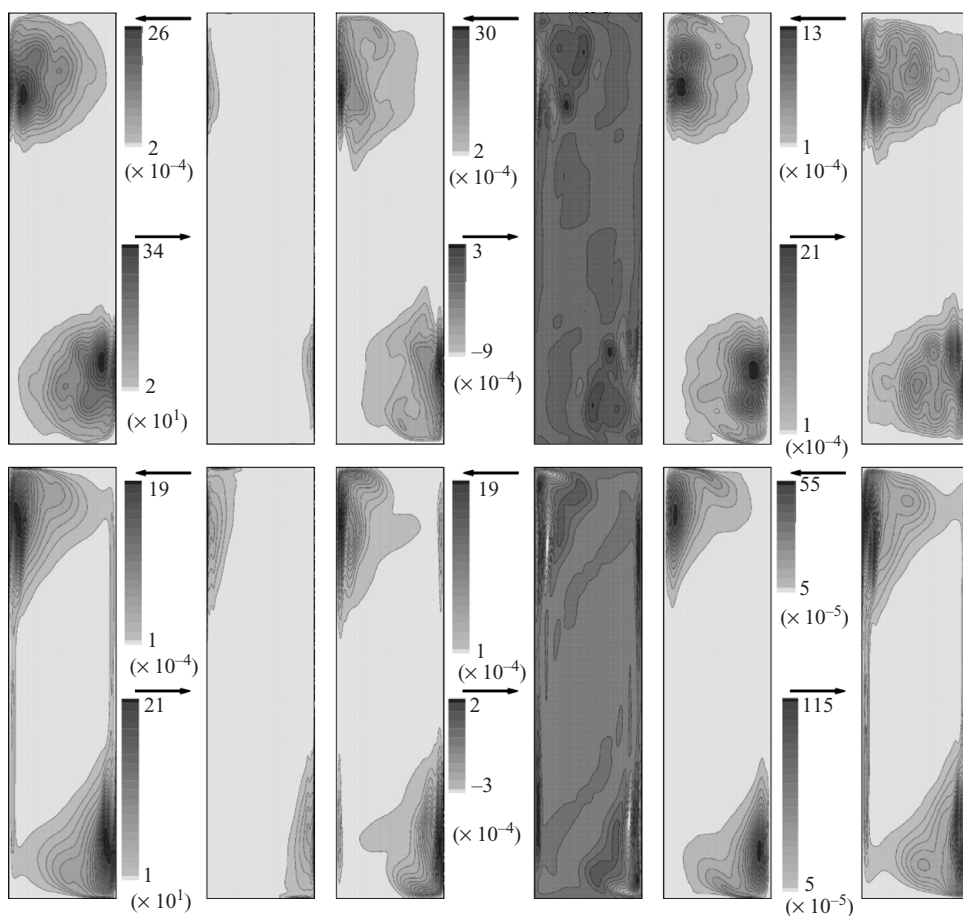


FIGURE 19. Second-order statistics at $Ra = 6.4 \times 10^8$, from left to right: k , ϵ_v , $\overline{T'T'}$, $\overline{u'_3T'}$, $\overline{u'_2u'_2}$ and $\overline{u'_3u'_3}$. Top: two-dimensional simulations. Bottom: three-dimensional simulations.

3.3.5. Second-order statistics

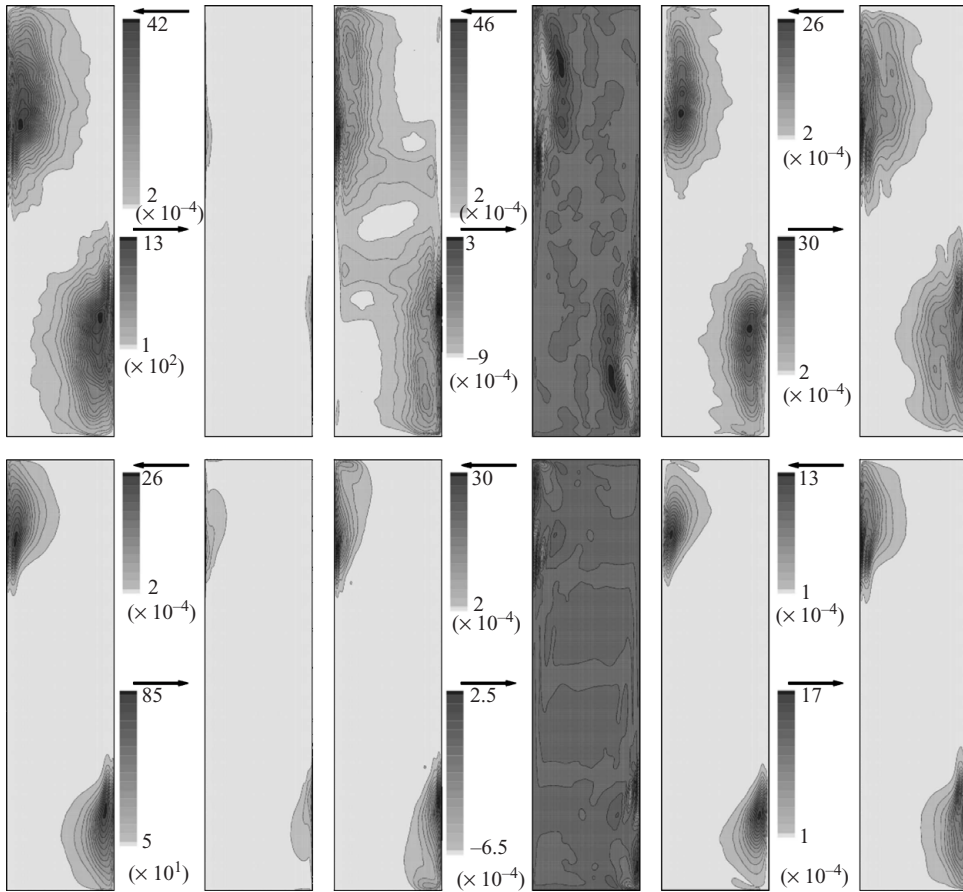
The distributions of turbulent kinetic energy $k = \overline{u'_i u'_i}$, its total viscous dissipation rate $\epsilon_v = \overline{(\nabla \mathbf{u}') : (\nabla \mathbf{u}')'}$, the temperature variance $\overline{T'T'}$, the turbulent heat flux $\overline{u'_3T'}$ and two of the four non-zero components of the Reynolds stress are shown in figures 19, to 21. It should be noted that, as the domain is homogeneous in the x_1 -direction, all the statistics are independent of x_1 , $\overline{u_1} = 0$, and the fluctuations of u_1 are uncorrelated with the fluctuations of other variables, i.e. $\overline{u'_1 u'_2} = \overline{u'_1 u'_3} = \overline{u'_1 T'} = 0$, except statistical noise that decreases with the integration period. Obviously, the component $\overline{u'_1 u'_1}$ vanishes for the two-dimensional simulations.

At $Ra = 6.4 \times 10^8$, the maxima and spatial distributions of the non-zero Reynolds stress tensor are already significantly different. For the two-dimensional results, as can be seen in figure 19, all the turbulent statistics are almost zero at the vertical boundary layers. In the two-dimensional case, the vertical boundary layers are almost steady, and the fluctuations are concentrated at the top and bottom regions, where the second-order statistics have more complex distributions than in the three-dimensional simulations (e.g. the maps of $\overline{u'_2 u'_2}$ obtained in the two-dimensional simulations also have a minimum at the corners, not present in the three-dimensional case). The

FIGURE 20. As figure 19, but for $Ra = 2 \times 10^9$.

two-dimensional and three-dimensional distributions of $\overline{u'_3 T'}$ are completely different. This behaviour is also observed in Soria *et al.* (2004).

In the top parts of figures 20 and 21, two-dimensional results at $Ra = 2 \times 10^9$ and $Ra = 10^{10}$, respectively, are presented. As expected, they are again in good agreement with Xin & Le Quéré (1995). Second-order statistics are only significant in the downstream part of the vertical boundary layers whereas the most upstream parts and most of the cavity core are laminar. Turbulent statistics and the region of large fluctuations increase with the Ra number. However, significant differences occur with the three-dimensional results (see also figures 20 and 21, bottom). At first sight we see that the spatial distribution of turbulent statistics differs substantially and that such differences become more evident when increasing the Ra number. At $Ra = 2 \times 10^9$, the three-dimensional results still display important fluctuations at the vertical boundary layer compared with the almost zero values of the two-dimensional counterpart. Viscous dissipation rate ϵ_v and the turbulent heat flux $\overline{u'_3 T'}$ are the statistics where this phenomenon is more evident. However, the most significant difference is that whereas for two-dimensional simulations the region of large fluctuations increases, for three-dimensional configurations it tends to decrease, shrinking to the two downstream corners. Thus, we conclude that flow anisotropy is even larger for three dimensions

FIGURE 21. As figure 19, but for $Ra = 10^{10}$.

where regions with high values of turbulent statistics coexist with a large laminar region. Such a phenomenon becomes clearly marked for the highest Rayleigh number results (see figures 21 and 22).

Since their physical origin is the same, the spatial correlations between different second-order statistics do not differ significantly between two-dimensional and three-dimensional simulations. Near the vertical walls, the non-slip boundary conditions for velocity make $\partial u'_3 / \partial x_2$ the leading term of the viscous dissipation rate ϵ_v , with its maxima located close to the wall, while k is essentially contributed by $\overline{u'_2 u'_2}$ whose maxima is located outside the boundary layer. This explains the bad correlation observed between two important quantities for turbulence modelling such as k and ϵ_v . The horizontal profiles at $x_3 = 0.8$, a region with high values of turbulent statistics, displayed in figure 22 show more clearly that these two quantities become more uncorrelated when Ra is increased.

3.4. Kinetic energy balances

The transport equation for kinetic energy, $e = (1/2)\mathbf{u} \cdot \mathbf{u}$ is obtained from the scalar product of velocity vector and momentum equation,

$$\frac{\partial e}{\partial t} = -\nabla \cdot (e\mathbf{u}) + \frac{Pr}{Ra^{0.5}} \nabla \cdot (\mathbf{u} \cdot (\nabla \mathbf{u} + \nabla \mathbf{u}^t)) - \frac{Pr}{Ra^{0.5}} \phi(\mathbf{u}) - \nabla \cdot (p\mathbf{u}) + \mathbf{u} \cdot \mathbf{f}, \quad (3.3)$$

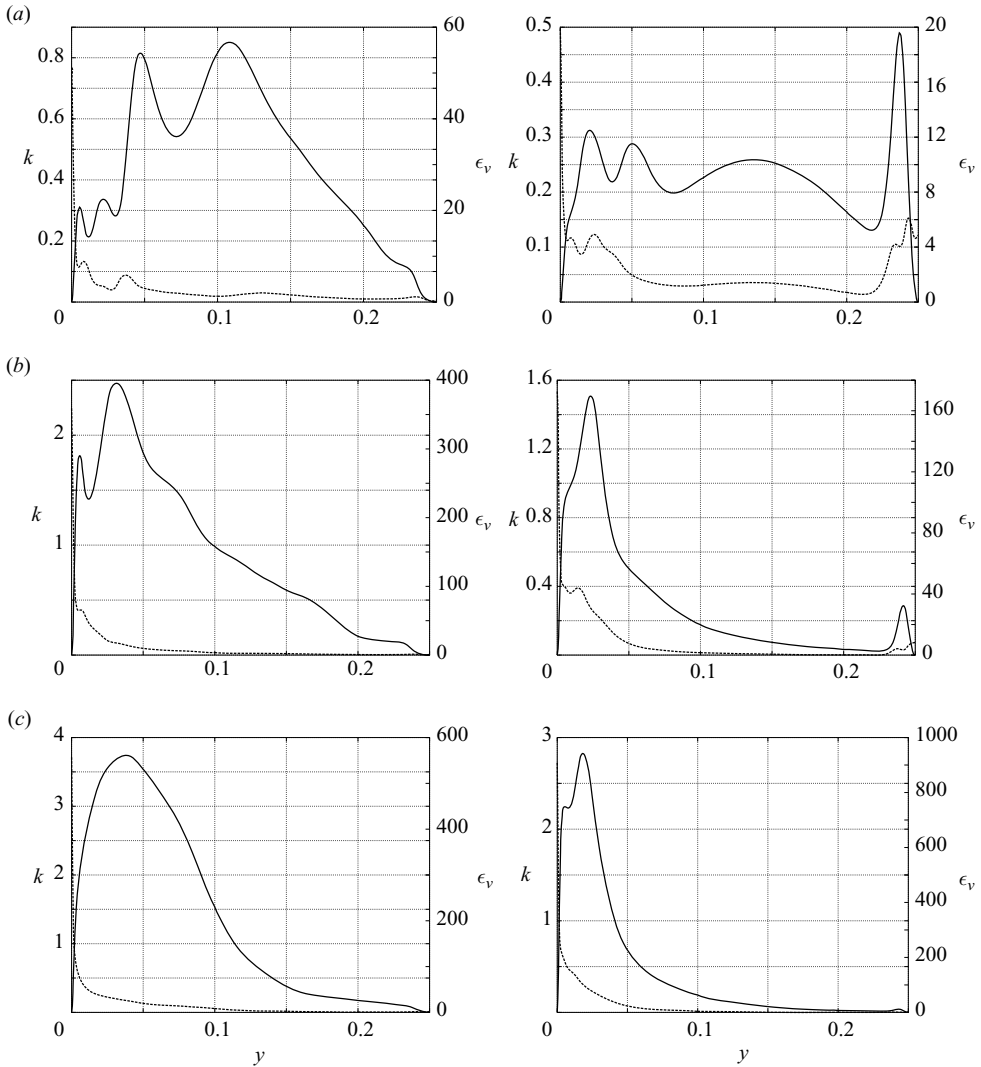


FIGURE 22. Horizontal profiles at $x_3 = 0.8$ of the turbulent kinetic energy k (solid line) and its viscous dissipation rate ϵ_v (dashed line): (a) $Ra = 6.4 \times 10^8$, (b) $Ra = 2 \times 10^9$ and (c) $Ra = 10^{10}$. Left: two-dimensional results. Right: three-dimensional results. The scale of k should be multiplied by 10^{-3} .

where $\phi(\mathbf{u}) = (\nabla \mathbf{u} + \nabla \mathbf{u}^t) : \nabla \mathbf{u}$. The term $-PrRa^{-0.5}\phi(\mathbf{u})$ is the kinetic energy dissipation rate that arises from the viscous forces term $PrRa^{-0.5}\nabla^2 \mathbf{u}$. Integration of (3.3) in the spatial domain Ω yields

$$\frac{dE_K}{dt} = \int_{\partial\Omega} \left(-e\mathbf{u} + \frac{Pr}{Ra^{0.5}} \mathbf{u} \cdot (\nabla \mathbf{u} + \nabla \mathbf{u}^t) + p\mathbf{u} \right) \cdot d\mathbf{S} + \int_{\Omega} \left(\mathbf{u} \cdot \mathbf{f} - \frac{Pr}{Ra^{0.5}} \phi(\mathbf{u}) \right) d\Omega, \quad (3.4)$$

where $E_K = \int_{\Omega} e d\Omega$ is the total kinetic energy. The first term, which accounts for the boundary interactions, is zero in domains where all the boundaries are either periodic or with zero velocity $\mathbf{u}|_{\partial\Omega} = \mathbf{0}$ (or a combination of both, as in our case). Considering these types of boundary conditions, the instantaneous global kinetic energy balance

equation can be expressed as

$$\frac{dE_K}{dt} = \int_{\Omega} \left(\mathbf{u} \cdot \mathbf{f} - \frac{Pr}{Ra^{0.5}} \phi(\mathbf{u}) \right) d\Omega = \int_{\Omega} \left(PrTu_3 - \frac{Pr}{Ra^{0.5}} \phi(\mathbf{u}) \right) d\Omega. \quad (3.5)$$

It is clear from this expression that the only term of the momentum equation that contributes to the evolution of the total kinetic energy is $-PrRa^{-0.5}\phi(\mathbf{u})$, which necessarily dissipates kinetic energy to thermal energy (as $\phi \geq 0$) and the body force term $\mathbf{u} \cdot \mathbf{f}$ that can either generate or dissipate kinetic energy. Pressure gradient and convective terms have a local effect, but do not contribute to the global kinetic energy balance. As the spectro-consistent numerical schemes by Verstappen & Veldman (2003), outlined in §2.2.1, used for the simulations do not introduce any artificial dissipation, the discrete velocity fields verify exactly the equality (3.5), even for very coarse meshes. This has been tested as an additional verification of the code.

Averaging (3.5), for a long enough time integration period, a global kinetic energy balance is obtained, which expressed per volume unit is given by

$$\underbrace{\frac{Pr}{V} \int_{\Omega} (\overline{u_3 T} + \overline{u'_3 T'}) d\Omega}_{\overline{E_g}} = \underbrace{\frac{Pr}{V Ra^{0.5}} \int_{\Omega} (\phi(\overline{\mathbf{u}}) + \overline{\phi(\mathbf{u'})}) d\Omega}_{\overline{E_d}}, \quad (3.6)$$

where V is the cavity volume. That is, for a statistically stationary flow, $\overline{E_g}$, the averaged kinetic energy generation rate (only due to the buoyancy forces in our case) must be equal to $\overline{E_d}$, the averaged kinetic energy dissipation rate due to viscous forces. Since the instantaneous kinetic energy balances are exactly satisfied, the energy imbalance expression $|\overline{E_g} - \overline{E_d}|/\overline{E_g}$ can be used to control whether averaging time is long enough. The values of $\overline{E_g}$ obtained in the different simulations can be found in table 6. At first sight, we see that the dimensionless overall kinetic energy generation rate $\overline{E_g}$ tends to decrease with the Rayleigh number following a correlation closer to $Ra^{-1/4}$. We also observe that slightly higher values are obtained for three-dimensional simulations. At §3.1, we saw that time-averaged temperature and vertical velocity profiles for different Rayleigh numbers collapse when the laminar $Ra^{1/4}$ scaling is used for lengths (see figure 8). We also saw that such laminar behaviour is exhibited in the upstream part of the boundary layers, where most of the kinetic energy is generated, and extends for more than half of the cavity. Thus, the $Ra^{1/4}$ scaling shown by the overall kinetic energy generation rate $\overline{E_g}$ is not surprising. With respect to the slightly higher values obtained for the three-dimensional simulations, such discrepancies probably occur because, as we saw in previous sections, the point where vertical boundary layers become totally disrupted moves downstream, resulting in a larger region of quasi-laminar behaviour.

In table 6, we also observe important discrepancies between two-dimensional and three-dimensional results for the turbulent dissipation term, $PrRa^{-0.5}/V \int_{\Omega} \phi(\mathbf{u'}) d\Omega$. Higher values are obtained for the three-dimensional simulations for the first two Rayleigh numbers, but a sudden decrease occurs for the three-dimensional results of the highest Rayleigh number. Meanwhile, the two-dimensional counterpart seems to go on growing with the Ra number. A reasonable explanation is that, as we saw in §3.3.5, for the two-dimensional simulations, when the Ra number is increased the regions with high turbulent fluctuations spread out, reducing the region of uniform stratification, whereas for the three-dimensional simulations, such regions seems to shrink to the two downstream corners of the cavity. Finally, turbulent generation term, $Pr/V \int_{\Omega} \overline{u'_3 T'} d\Omega$ displays completely different tendencies. It seems clear that it

Case	Ra	$\overline{E_g} = \overline{E_d}$	$\frac{Pr}{V Ra^{0.5}} \int_{\Omega} \overline{\phi(u')} d\Omega$	$\frac{Pr}{V} \int_{\Omega} \overline{u'_3 T'} d\Omega$	$\overline{E_g} Ra^{1/4}$
AA2D	6.4×10^8	1.976×10^{-3}	3.89×10^{-5}	1.81×10^{-7}	0.314
BB2D	2×10^9	1.491×10^{-3}	6.39×10^{-5}	-9.39×10^{-7}	0.315
CC2D	10^{10}	1.002×10^{-3}	8.04×10^{-5}	-1.65×10^{-5}	0.317
A	6.4×10^8	1.996×10^{-3}	5.33×10^{-5}	4.71×10^{-6}	0.317
B	2×10^9	1.524×10^{-3}	8.08×10^{-5}	2.36×10^{-6}	0.322
C	10^{10}	1.023×10^{-3}	6.67×10^{-5}	2.41×10^{-7}	0.323

TABLE 6. Global kinetic energy balances.

tends to decrease with Ra number; however, this reduction is more marked for the two-dimensional simulations, obtaining negative values of turbulent generation term for the two highest Rayleigh numbers. It is necessary to perform simulations at higher Rayleigh numbers to confirm these tendencies.

4. Conclusions

A set of complete two- and three-dimensional direct numerical simulations of a buoyancy-driven flow in a differentially heated air-filled ($Pr=0.71$) cavity of aspect ratio 4 and Rayleigh numbers up to 10^{10} has been presented. The correctness of the code has been verified using the method of manufactured solutions, which ensures that the order of accuracy is in good agreement with the theoretical expectation in the whole domain. A low-cost parallel computer (a PC cluster with a conventional 1 Gbits/s network) has been used for the simulations. An explicit scheme has been used for temporal integration and second- and fourth-order schemes for spatial discretization. These schemes preserve the global kinetic energy balances, even for very coarse meshes. The parallel algorithm is based on spatial domain decomposition. A direct algorithm (DSFD) has been used to solve the Poisson equations with only one communication episode. The main features of the flow, including the time-averaged flow structure, the power spectra and probability density distributions of a set of selected monitoring points, the turbulent statistics, the global kinetic energy balances and the internal waves motion phenomena, have been presented and compared.

All simulations share some basic flow features: a stratified cavity core, recirculating structures near the downstream corners and thin vertical boundary layers that remain laminar at their upstream part up to a point above the mid-height where transition occurs. Periodic oscillations are amplified in the boundary layer and trigger nonlinear effects provoking the transition. With respect to the centreline dimensionless thermal stratification, all the numerical simulations performed in this work give values close to 1 whereas experimental studies yield values of about 0.5. These results confirm the conclusions of Salat *et al.* (2004) discarding the three-dimensional effects as a possible reason for these discrepancies. Understanding the origins of these differences seems an interesting area for future work.

With respect to the comparison between two- and three-dimensional results, the time-averaged flow structures are similar, in particular the averaged local and overall Nusselt numbers. However, significant differences are observed in the flow dynamics. For two-dimensional simulations, the oscillations at the downstream part of the boundary layer are clearly stronger, ejecting large unsteady eddies to the cavity core where the isotherms exhibit a periodical motion around the mean horizontal position.

In the three-dimensional simulations, these eddies do not persist and their energy is rapidly passed down to smaller scales of motion causing an evident reduction of the large-scale mixing effect at the hot upper and cold lower regions and consequently a still almost motionless stratified cavity core is displayed. The boundary layers remain laminar or quasi-laminar on their upstream parts, up to the point where these eddies are ejected. The point where this phenomenon occurs clearly moves to a more upstream location for the three-dimensional simulations. All these differences become more marked for the highest Rayleigh number. It is also shown that, even for the three-dimensional simulations, these eddies are large enough to permanently excite an internal wave motion oscillating at the Brunt–Väisälä frequency in the stratified core region.

For the range of Rayleigh number investigated here, second-order statistics are significant only on the downstream corners of the cavity. The assumption of instantaneous two-dimensional maps clearly influences the distribution of all the second-order statistics, that are substantially different (by two orders of magnitude in certain cases). For the lowest Rayleigh number, the main differences occur at the vertical boundary layers, where the two-dimensional simulation incorrectly predicts low values for all the second-order statistics. However for the two highest Ra numbers, the differences become more marked: whereas the area of large fluctuations tends to increase for two-dimensional simulations, for the three-dimensional configuration it decreases, shrinking to the two downstream corners. Spatial correlations of second-order statistics are qualitatively similar for all simulations. In the context of turbulence modelling, the bad correlation between k and ϵ_v is especially significant.

We can conclude that two-dimensional simulations may be enough, as a first and cheaper approach, to capture the general features of buoyancy-driven flows in enclosed cavities at Rayleigh numbers up to 10^{10} . However, three-dimensional simulations are necessary for an accurate description of the flow, specially for turbulent statistics. This issue could be relevant if DNS is to be used to develop or enhance turbulence modelling.

This work has been financially supported by the ‘Ministerio de Educación y Ciencia’, Spain; contract/grant number ENE2006-14247.

REFERENCES

- BETTS, P. L. & BOKHTARI, I. H. 2000 Experiments on turbulent natural convection in an enclosed tall cavity. *Intl J. Heat Fluid Flow* **21**, 675–683.
- CHORIN, A. J. 1968 Numerical solution of the Navier–Stokes equations. *J. Comput. Phys.* **22**, 745–762.
- CHORIN, A. J. 1993 *A Mathematical Introduction to Fluid Mechanics*. Springer.
- CHRISTON, M. A., GRESHO, P. M. & SUTTON, S. B. 2002 Computational predictability of time-dependent natural convection flows in enclosures (including a benchmark solution). *Intl J. Numer. Meth. Fluids* **201**, 953–980.
- FARHANGNIA, M., BIRINGEN, S. & PELTIER, L. 1996 Numerical simulation of two-dimensional buoyancy-driven turbulence in a tall rectangular cavity. *Intl J. Numer. Meth. Fluids* **23**, 1311–1326.
- FUSEGI, F., FAROUK, B., HYUN, J. M. & KUWAHARA, K. 1990 A direct numerical simulation of periodic natural convection in differentially heated cubical enclosure. In *Proc. Intl Symp. on Engineering Turbulence Modeling and Measurements*, pp. 261–268.
- FUSEGI, T., HYUN, J., KUWAHARA, K. & FAROUK, B. 1991 A numerical study of three-dimensional natural convection in a differentially heated cubical enclosure. *Intl J. Heat Mass Transfer* **34**, 1543–1557.

- FUSEGI, T., HYUN, J. M. & KUWAHARA, K. 1992 Three-dimensional numerical simulation of periodic natural convection in differentially heated cubical enclosure. *Appl. Sci. Res.* **49**, 271–282.
- HENKES, R. 1995 Natural-convection boundary layers. PhD thesis, Faculty of Applied Physics, Delft University of Technology.
- HENKES, R. A. W. M. & LE QUÉRÉ, P. 1996 Three-dimensional transition of natural-convection flows. *J. Fluid Mech.* **319**, 281–303.
- HORTMANN, M., PERIC, M. & SCHEUERER, G. 1990 Finite volume multigrid prediction of laminar natural convection: bench-mark solutions. *Intl J. Numer. Meth. Fluids* **11**, 189–207.
- JANSEN, R. J. A. & HENKES, R. A. W. M. 1996 Instabilities in three-dimensional differentially-heated cavities with adiabatic horizontal walls. *Phys. Fluids* **8** (1), 62–74.
- JANSEN, R. J. A., HENKES, R. A. W. M. & HOOGENDOORN, C. J. 1993 Transition to time-periodicity of a natural-convection flow in a 3-D differentially heated cavity. *Intl J. Heat Mass Transfer* **36** (11), 2927–2940.
- KRAICHNAN, R. H. 1967 Inertial-ranges in two-dimensional turbulence. *Phys. Fluids* **10**, 1417–1423.
- LABROSSE, G., TRIC, E., KHALLOUF, H. & BETROUNI, M. 1997 A direct (pseudo-spectral) solver of the 2-D/3-D Stokes problem: transition to unsteadiness of natural-convection flow in a differentially heated cubical cavity. *Numer. Heat Transfer B* **31**, 261–276.
- LARTIGUE, B., LORENTE, S. & BOURRET, B. 2000 Multicellular natural convection in a high aspect ratio cavity: experimental and numerical results. *Intl J. Heat Mass Transfer* **43**, 3157–3170.
- LE QUÉRÉ, P. 1990 A note on multiple and unsteady solutions in two-dimensional convection in a tall cavity. *J. Heat Transfer* **112**, 965–974.
- LE QUÉRÉ, P. 1991 Accurate solutions to the square thermally driven cavity at high rayleigh number. *Computers Fluids* **20**, 29–41.
- LE QUÉRÉ, P. 1994 Transition to unsteadiness routes to chaos and simulation of turbulent flows in cavities heated from the side: a review of present status. In *Heat Transfer: Proceedings of the 10th Intl Heat Transfer Conf.*, vol. 1, pp. 281–296. Hewitt GF.
- LE QUÉRÉ, P. & BEHNIA, M. 1998 From onset of unsteadiness to chaos in a differentially heated square cavity. *J. Fluid Mech.* **359**, 81–107.
- LIGHTHILL, J. 2002 *Waves in Fluids*. Cambridge University Press.
- PAOLUCCI, S. 1990 Direct numerical simulation of two-dimensional turbulent natural convection in an enclosed cavity. *J. Fluid Mech.* **215**, 229–262.
- PAOLUCCI, S. & CHENOWETH, D. R. 1989 Transition to chaos in a differentially heated vertical cavity. *J. Fluid Mech.* **201**, 379–410.
- PENOT, F., N'DAME, A. & LE QUÉRÉ, P. 1990 Investigation of the route to turbulence in a differentially heated cavity. In *9th Intl Heat Transfer Conference*, pp. 417–422. Jerusalem.
- RAVI, M., HENKES, R. & HOOGENDOORN, C. 1994 On the high-Rayleigh-number structure of steady laminar natural-convection flow in a square enclosure. *J. Fluid Mech.* **262**, 325–351.
- ROACHE, P. J. 2002 Code verification by the method of manufactured solutions. *Trans. ASME I: J. Fluids Engng* **124**, 4–10.
- SALAT, J., XIN, S., JOUBERT, P., SERGENT, A., PENOT, F. & LE QUÉRÉ, P. 2004 Experimental and numerical investigation of turbulent natural convection in large air-filled cavity. *Intl J. Heat Fluid Flow* **25**, 824–832.
- SCHWEIGER, H., OLIVA, A., COSTA, M. & PÉREZ-SEGARRA, C. D. 1995 Numerical experiments on laminar natural convection in rectangular cavities with and without honeycomb structures. *Intl J. Numer. Meth. Heat Fluid Flow* **5**, 243–443.
- SORIA, M., PÉREZ-SEGARRA, C. D. & OLIVA, A. 2002 A direct parallel algorithm for the efficient solution of the pressure-correction equation of incompressible flow problems using loosely coupled computers. *Numer. Heat Transfer B* **41**, 117–138.
- SORIA, M., PÉREZ-SEGARRA, C. D. & OLIVA, A. 2003 A direct Schur–Fourier decomposition for the solution of the three-dimensional poisson equation of incompressible flow problems using loosely parallel computers. *Numer. Heat Transfer B* **43**, 467–488.
- SORIA, M., TRIAS, F. X., PÉREZ-SEGARRA, C. D. & OLIVA, A. 2004 Direct numerical simulation of a three-dimensional natural-convection flow in a differentially heated cavity of aspect ratio 4. *Numer. Heat Transfer A* **45**, 649–673.
- TIAN, Y. S. & KARAYIANNIS, T. G. 2000a Low turbulence natural convection in an air filled square cavity. Part I: the thermal and fluid flow fields. *Intl J. Heat Mass Transfer* **43**, 849–866.

- TIAN, Y. S. & KARAYIANNIS, T. G. 2000*b* Low turbulence natural convection in an air filled square cavity. Part II: the turbulence quantities. *Intl J. Heat Mass Transfer* **43**, 867–884.
- TRIAS, F. X., SORIA, M., OLIVA, A. & VERSTAPPEN, R. 2006*a* Regularization models for the simulation of turbulence in a differentially heated cavity. In *Proc. European Comput. Fluid Dynamics Conference (ECCOMAS CFD 2006)*. Egmond aan Zee, The Netherlands.
- TRIAS, F. X., SORIA, M., PÉREZ-SEGARRA, C. D. & OLIVA, A. 2006*b* A direct Schur–Fourier decomposition for the efficient solution of high-order poisson equations on loosely coupled parallel computers. *Numerical Linear Algebra with Applications* **13**, 303–326.
- TRIC, E., LABROSSE, G. & BETROUNI, M. 2000 A first incursion into the 3D structure of natural convection of air in a differentially heated cubic cavity. *Intl J. Heat Mass Transfer* **43**, 4043–4056.
- DE VAHL DAVIS, G. & JONES, I. P. 1983 Natural convection in a square cavity: a comparison exercise. *Intl J. Numer. Meth. FLuids* **3**, 227–248.
- VERSTAPPEN, R. 2007 On restraining the production of small scales of motion in a turbulent channel flow. *Computers Fluids* (to appear).
- VERSTAPPEN, R. & VELDMAN, A. 1997 Direct numerical simulation of turbulence at lower costs. *J. Engng Maths* **32**, 143–159.
- VERSTAPPEN, R. W. C. P. & VELDMAN, A. E. P. 1998 Spectro-consistent discretization of Navier–Stokes: a challenge to RANS and LES. *J. Engng Maths* **34**, 163–179.
- VERSTAPPEN, R. W. C. P. & VELDMAN, A. E. P. 2003 Symmetry-preserving discretization of turbulent flow. *J. Comput. Phys.* **187**, 343–368.
- WAN, D., PATNAIK, B. & WEI, G. 2001 A new benchmark quality solution for the buoyancy-driven cavity by discrete singular convolution. *Numer. Heat Transfer B* **40**, 199–228.
- WINTERS, K. H. 1987 Hopf bifurcation in the double-glazing problem with conducting boundaries. *J. Heat Transfer* **109**, 894–898.
- XIN, S. & LE QUÉRÉ, P. 1995 Direct numerical simulations of two-dimensional chaotic natural convection in a differentially heated cavity of aspect ratio 4. *J. Fluid Mech.* **304**, 87–118.
- XIN, S. & LE QUÉRÉ, P. 2002 An extended chebyshev pseudo-spectral benchmark for the 8:1 differentially heated cavity. *Intl J. Numer. Meth. Fluids* **8**, 2182–2189.
- YANENKO, N. N. 1971 *The Method of Fractional Steps*. Springer.